

THE POPULATION OF COMPACT RADIO SOURCES IN M 17

Vanessa Yanza^{1,2}, Josep M. Masqué¹, Sergio A. Dzib³, Luis F. Rodríguez², S.-N.X. Medina³, Stan Kurtz², Laurent Loinard², Miguel A. Trinidad¹, Karl M. Menten³, Carlos A. Rodríguez-Rico¹

ABSTRACT

We present a catalog of radio sources of the M 17 region based on deep X band radio observations centered at 10 GHz obtained with the Jansky Very Large Array in the A configuration. We detect a total of 194 radio sources, 12 of them extended and 182 compact. We find that a significant fraction (at least 40% in our catalog) have suspected gyrosynchrotron emission associated with stellar coronal emission. By comparing the radio luminosities of our sources with their X ray counterparts, when available, we find that they are underluminous in X rays with respect to the Güdel Benz relation, but a correlation with a similar slope is obtained provided that only sources with evident non thermal nature are selected from the sample compiled for the Orion Nebula Cluster (ONC) and M17. The comparison of M17 with the ONC and NGC 6334D-F leads to a similar luminosity function for the three regions, at least for the more luminous sources. However, the radio sources in M17 are three times more numerous compared to the other regions at a given luminosity and their spatial distribution differs from that of Orion. Moreover, an arc-shaped structure of 40'' in extent is observed in our map, identified previously as an ionizing front, with the cometary Hyper Compact source UC1 at its focus. Archival 1 mm ALMA data reveals compact emission coincident with the radio wavelength peak, possibly associated with a protostellar disk of the massive star exciting UC1.

Subject headings: Radio Source Catalog - Star Forming Regions - Young Stellar Objects (YSO)

1. Introduction

The Messier 17 (M17) region (the Omega Nebula, Horseshoe Nebula, Swan Nebula, Checkmark Nebula, W 38, S 45 or NGC 6618) is a bright HII region associated with a giant molecular cloud located in the Sagittarius constellation at a distance of $1.98_{-0.12}^{+0.14}$ kpc (Wu et al. 2014). The complex is considered one of the most massive and luminous regions of recent star formation in the Milky Way (Lada et al. 1974). It is composed of a main star-forming region located between two bars situated to the North (N-bar) and to the South (S-bar, Felli et al. 1980). This region has an associated open

stellar cluster (Beetz et al. 1976; Morales et al. 2013) whose most luminous object is the massive multiple system CEN 1 (Chini et al. 1980). The main components of this system, CEN 1a and CEN 1b (Hoffmeister et al. 2008) with nearly equal masses, have been detected at several wavelengths and found to be time variable in some of them (Broos et al. 2007; Rodríguez et al. 2009).

The cluster ionizes the surrounding interstellar medium (ISM) so that a large arc-shaped structure is formed (Felli et al. 1980; Johnson et al. 1998) that is associated with an ionization front. Beyond this limit the material of the cloud is mostly molecular (Felli et al. 1980, 1984). At the focus of the arc structure there is a very radio-bright Hyper-Compact HII (HCHII) region called UC1 (Felli et al. 1980). Many studies dedicated to this source show that it is associated with a disk-like structure and masers (Johnson et al. 1998; Niel-

¹Departamento de Astronomía, Universidad de Guanajuato, Apdo. Postal 144, 36000 Guanajuato, México

²Instituto de Radioastronomía y Astrofísica, Universidad Nacional Autónoma de México, Morelia 58089, México

³Max Planck Institut für Radioastronomie, Auf dem Hügel 69, D-53121 Bonn, Germany

bock et al. 2007) among other features. Given the peculiar location of UC1 with respect to the ionization front, Felli et al. (1984) and Johnson et al. (1998) discuss the possibility of shock-induced star formation occurring in this source.

The large luminosity of M 17 ($\sim 10^7 L_{\odot}$) and its extended size (up to 1° considering the molecular environment, see Elmegreen et al. 1977), together with the wealth of structures found within, motivated many surveys of the region at multiple wavelengths. At IR and optical bands, following the early survey of Chini et al. (1980), the population of massive and intermediate mass young objects came to light in the subsequent surveys (Chini & Kruegel 1985; Chini & Wargau 1998; Hanson et al. 1997; Nielbock et al. 2007). Moreover, deeper observations show that beyond the central cluster of massive stars, additional generations of young stellar objects populating other parts of the complex are present (Jiang et al. 2002; Chini et al. 2004; Povich et al. 2009). This stellar richness was confirmed by Broos et al. (2007) with X-ray observations, which detected 886 sources around M 17 covering a wide field. At radio wavelengths, Rodríguez et al. (2012, hereafter RGM2012) detected 38 compact radio sources, 19 of them with stellar counterparts. These 38 sources constitute the most extensive catalog of radio sources in M 17 to date.

Because star forming regions are embedded in dense molecular clouds, radio emission counterparts provide information on the most obscured objects associated to the region. Furthermore, since the whole region is a strong radio emitter due to the extended gas ionized by massive stars, interferometric observations are crucial to isolate and explore the most compact parts. Such observations reveal the presence of a rich variety of types of radio sources, some of them individual and compact, suggesting that they are associated with young objects embedded in the parental nebula; many of them are not detected at any other wavelength.

The radio emission of these Compact Radio Sources (CRSs) can be thermal and/or non-thermal. The former is produced by free-free emission from ionized gas present in Hyper-Compact (HC)HII regions surrounding OB stars, ionized winds of massive stars, externally ionized protoplanetary disks (proplyds) or jets from low-mass

protostars (Panagia & Felli 1975; Shull 1980; Avalos et al. 2009; Sánchez-Monge et al. 2011; Zapata et al. 2004; Stecklum et al. 1998; Reynolds 1986; Anglada et al. 2018). On the other hand, non-thermal radio emission is generated by relativistic charged particles moving in a magnetic field. This emission can be produced by gyrosynchrotron processes occurring in low-mass stars with superficial magnetic fields, or synchrotron processes due to the collision between winds of massive binary stars, among other possibilities (Feigelson & Montmerle 1999; Dzib et al. 2015; Dougherty & Williams 2000; Blomme et al. 2013).

The extended family of possible radio emitting objects described above implies a wide range of radio flux density expected for them. As a consequence, weak sources found at the lower end of this range become potentially undetectable and surveys might be biased to strong sources (Medina et al. 2019; Brunthaler et al. 2021). This has been alleviated in recent years thanks to the upgraded instrumentation installed on radio interferometers. This enables deep studies of star forming regions, that have notably increased the number of detected CRSs. Using one of the most important instruments, the Very Large Array (VLA), several studies were conducted of different HII regions and very faint CRSs were detected. For example, early surveys of the Orion Nebula reported ~ 20 radio sources of a few mJy of flux density (Churchwell et al. 1987; Garay et al. 1987). Zapata et al. (2004) later increased the cataloged sources to 77 and found that a significant fraction of CRSs show time variability. Recently, Forbrich et al. (2016) presented the deepest observations ever performed on Orion using the same instrument, upgraded to the *Karl G. Jansky* Very Large Array and detected 556 radio sources of differing nature. The Nebula NGC 6334, a string of star forming regions of different evolutionary status, including several HII regions, was studied recently by Medina et al. (2018) who cataloged 83 CRSs; only a few were previously known. Despite the larger distances of other regions as compared to Orion, in general, sufficiently deep observations of star forming regions show a significant increase in radio source detections compared to the old catalogs. This suggests that a rich population of radio sources exists in many regions of star formation; in most cases, this rich population remains to be

uncovered.

Following previous radio observations of the M 17 region (RGM2012), we carried out a study toward this region with the upgraded VLA. We achieve a significantly better sensitivity in our maps than in previous observations. This allows us to very significantly expand the radio source catalog of the M 17 region by exploring the weakest radio components yet detected in the region. Furthermore, we analyze the nature of the population of radio sources using methods developed in other regions. In Section 2, we describe the observations and present the final map after the self-calibration process. In Section 3, we present the catalog of CRSs extracted from the final map. An analysis of the properties of CRSs extracted from the map is presented in Section 4. In Section 5, we constrain the nature of the CRSs and discuss their implications for the region. Finally, in Section 6 we draw our conclusions.

2. Observations

The VLA data were taken using the most extended A configuration in the X band (8-12 GHz) toward the M 17 star forming region. The pointing center was $\alpha(\text{J2000}) = 18^{\text{h}}20^{\text{m}}30^{\text{s}}$ and $\delta(\text{J2000}) = -16^{\circ}10'45''$ and the Full Width Half Maximum (FWHM) of the primary beam at the center of the band was $5'$ (though it varies significantly over the 4 GHz bandwidth). The observations were made in three epochs with a total observation time of four hours (one hour on 2018 May 3, one hour on May 4 and two hours on May 8). The data were taken using the 3-bit sampling mode with an integration time set to 2 seconds. The correlator was configured to 4 GHz of continuous bandwidth coverage in full polarization mode, divided into 32 contiguous spectral windows, each with 64 channels of 2 MHz. The quasar 3C 286 was used as flux reference and bandpass calibrator, and J1832-1032 was used for the gain calibration. The theoretical noise of the combined observations is $2.6 \mu\text{Jy beam}^{-1}$ and the expected synthesized beam is $\sim 0''.2$.

The data were edited, calibrated and imaged using the Common Astronomy Software Applications package, CASA (McMullin et al. 2007). An

initial calibration and basic flagging were done following standard procedures. We combined the data of the three epochs into a single initial map using a weighting of $\text{robust} = -0.5$. This provided a map with a beam size of $\sim 0''.2$ and an rms noise of $27 \mu\text{Jy beam}^{-1}$. As this noise level was still far from the expected theoretical noise, we self-calibrated the combined data using the brightest source in the region, the UC1 source, assuming that this source does not vary significantly over the three observing days (RGM2012). In this process we applied two calibrations in phase, followed by one in amplitude and, finally, one more in phase. This improved the noise level of the map to $5 \mu\text{Jy beam}^{-1}$. This final map, which was primary beam-corrected, is shown in Fig. 1. Although the different primary beam function between the 9 and 11 GHz maps must bias the source detection toward sources with negative spectral indices, this effect is specially notable toward the outskirts of the map. Therefore, we adopted the FWHM of the primary beam at 9 GHz as the limiting size of the region where the spectral indices are trustable, which includes the majority of our sources. Moreover, most sources are gathered around the map center (i.e. in the HII region) where this effect is probably not significant.

3. Results

3.1. Source Extraction

We extracted sources from the final map using the BLOBCAT software (Hales et al. 2012). This software has been successfully used to do source extractions from radio images of other star forming regions (e.g., Medina et al. 2018) and from radio surveys covering significantly larger areas of the sky (e.g., Bühr et al. 2016; Medina et al. 2019). We follow a similar method to those used in these previous works which we briefly describe below.

BLOBCAT extracts information of islands of pixels using the flood fill algorithm in 2D astronomical images. It applies bias corrections to Gaussian and non-Gaussian sources to obtain accurate measurements. This allows us to perform an automatic extraction of radio sources and determine some of their observational properties. To correctly run the extraction, the Graphical Astronomy and Imaging Analysis Tool (GAIA, based on SEXtractor; Bertin & Arnouts 1996; Holw-

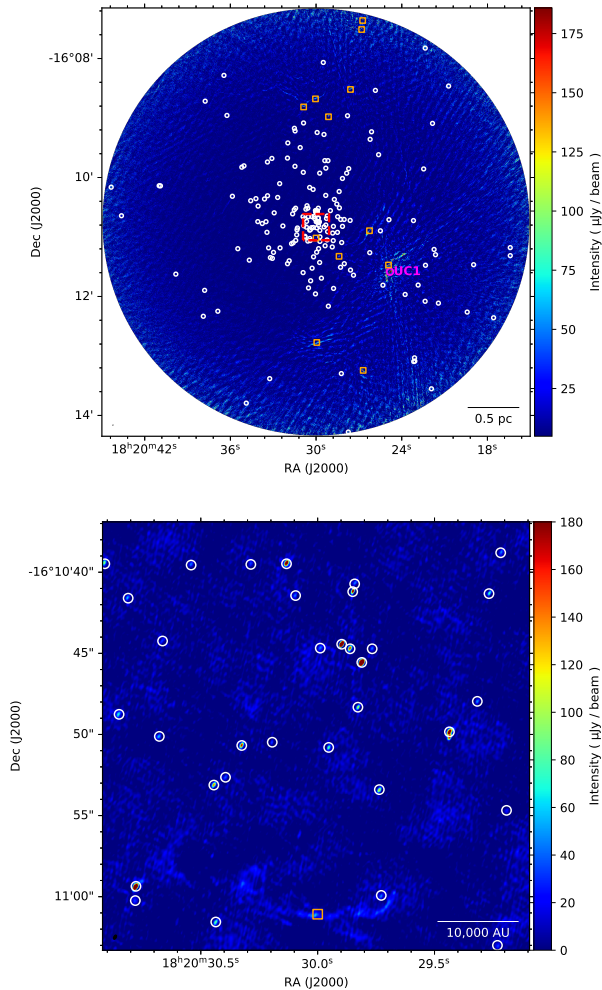


Fig. 1.— *Top panel:* VLA radio continuum map of the M17 region (color scale) using the A configuration and X band (8 – 12 GHz). The noise at its center is $5 \mu\text{Jy beam}^{-1}$. The synthesized beam is $0''.285 \times 0''.152$, P.A. = $-28^\circ.77$. White circles represent the position of the compact radio sources detected. Orange squares reveal the position of the peak of the extended sources. The magenta circle represents the position of the brightest source, UC1. The increased noise at the outer edge of the image is due to the correction for the primary beam response. There is also increased noise in the surroundings of UC1. The dashed red box represents the area shown enlarged in the bottom panel. The full FITS image is available upon request to jmasque@ugto.mx. *Bottom panel:* Zoom-in image of the central area of the observed field. Symbols are the same as in the top panel. The beam is the same as in the top panel and shown in the bottom left corner.

erda 2005) software was used to generate an *rms* noise 2D map of the data. To obtain the background noise map, the chosen Photometry type and Checkimage were “Background RMS” and “Full res. noise background”, respectively with a minimum island size of 5 pixels and a mesh size of 70 (see Hales et al. 2012). This noise map was then used with a signal to noise ratio of 5 (i.e., setting the *dSNR* parameter of BLOBCAT to 5σ) for the processing over our M17 map. With these parameters BLOBCAT extracts 200 preliminary radio sources.

3.2. Extragalactic sources and false detections

The expected number of background extragalactic sources in the imaged area was obtained using the equation below taken from Anglada et al. (1998). In this expression, θ_F is the angular diameter of the observed field, ν is the central frequency and S_o is the minimum detected flux density at the field center. These values were set to $7.2'$, 10 GHz, and 0.025 mJy, respectively.

$$\langle N \rangle = 1.4 \left\{ 1 - \exp \left[-0.0066 \left(\frac{\theta_F}{\text{arcmin}} \right)^2 \left(\frac{\nu}{5 \text{ GHz}} \right)^2 \right] \right\} \left(\frac{S_o}{\text{mJy}} \right)^{-0.75} \left(\frac{\nu}{5 \text{ GHz}} \right)^{-2.52} \quad (1)$$

This equation gives the expected number of extragalactic sources of $\langle N \rangle = 3 \pm 2$. In addition, using the statistical equation 1 from Medina et al. (2018), the maximum expected number of false detections is 5. This suggests that a maximum of about 10 sources from the BLOBCAT outcome are artifacts or extragalactic sources. In consequence, almost all of the sources we catalog are real and potentially belong to the M17 region.

3.3. Final catalog

We visually inspected the BLOBCAT detections, defining them as compact or extended sources. We classify as extended sources those that have an irregular resolved morphology, and as compact those with an approximately Gaussian shape and a single well-defined peak. Typical sizes for compact radio sources (CRSs) are not larger than a fraction of an arcsec. In some cases BLOBCAT detected several contiguous sources that are

part of a single large structure. Specifically, 4 extended sources were comprised of 9 sources extracted by BLOBCAT. For these extended sources we re-measured the flux density using CASA tools, considering each one as a single source. Moreover, we rejected 2 likely spurious sources by visual inspection, e.g. sources at the edge of the map where the *rms* noise level is high enough to create unreal sources. As a result, we retained 12 extended sources and 182 compact radio sources. These results are summarized in Table 1.

Table 2 shows the properties of the extended sources, namely their position (centered in the source emitting area), the peak flux, integrated flux density and angular area of each source measured by IMSTAT from CASA using contours of 5σ . Sources 6 and 10 have been detected before by RGM2012 with their C band observations and are labeled 11 and 18 in their catalog, respectively. Their reported sizes are $0''.4$ and $0''.6$. Our measured sizes for these sources are approximately $1''.3 \times 0''.4$ and $3''.7 \times 2''.2$. This difference is likely due to the different sensitivity between the observations.

3.4. Counterparts at other wavelengths

We searched for counterparts at other wavelengths cross-matching our CRSs using the SIMBAD database. The maximum discrepancy tolerance in position between our CRSs and the X-ray counterparts was $0''.8$. For IR, optical and radio wavelengths it was $0''.75$. These limits include the astrometric uncertainty our VLA map and our fit, and the approximate position errors in the counterpart. In Table 8 (see Appendix A) we indicate the counterparts of our CRSs and their respective detected band.

We searched the Gaia catalog for counterparts to the radio sources identified in our survey. Table 3 lists the sources with Gaia counterparts, their parallax and distances. The errors on the distances were calculated using standard error propagation. We find that six of the sources have distances discrepant from that of M17 ($d = 1.98$ kpc) by more than two sigmas. These are sources with number 8, 27, 40, 110, 128 and 170. These sources are likely to be foreground objects, rather than sources associated with M17 itself. In the following, we exclude these sources our analysis.

4. Analysis

In order to characterize the nature of the CRSs, we explored basic physical properties, namely spectral index, variability and polarization. The spectral index is a valuable preliminary diagnostic to assess whether the radio emission from a given source is of thermal or non thermal nature. Spectral indices below -0.1 indicate undoubtedly non-thermal nature (Rodríguez et al. 1993). On the other hand, spectral indices above this limit are expected for thermal sources with the caveat that gyrosynchrotron emission can result in spectral indices up to 2.5. This latter emission implies non-thermal processes occurring usually on the stellar surfaces of young objects (e.g., magnetic reconnection events, Dulk 1985; Feigelson & Montmerle 1999). Besides, extragalactic sources are usually optically-thin emitters and their spectral indices can be mimicked by gyrosynchrotron sources (e.g., Fleishman & Melnikov 2003; Forbrich et al. 2016; Wang et al. 2018). However, as seen in the previous section, the number of extragalactic sources in our catalog of CRS is not statistically significant. As we discuss in Sect. 5, two important properties are associated with gyrosynchrotron emission: rapid variability and circular polarization.

4.1. Spectral index

We estimated spectral indices of our CRSs dividing our data into two frequency intervals of 2 GHz and imaged each one in independent maps of 16 spectral windows. The maps have central frequencies of 9 GHz and 11 GHz, and noise levels of $11 \mu\text{Jy beam}^{-1}$ and $9 \mu\text{Jy beam}^{-1}$, respectively. Using BLOBCAT again, we determined the flux density of the CRSs belonging to each map and calculated their spectral indices. Most of the spectral indices were not well constrained due to the narrow frequency separation, causing large errors. Hence, in Table 4 we list the sources whose spectral indices have errors ≤ 0.5 , as well as their flux density at 9 and 11 GHz. We note that negative spectral indices are dominant. Given that most sources are found at the center of the map (see Fig. 1), this can not be an effect of the primary beam difference between the 9 and 11 GHz maps.

Table 1: Summary of the source selection process to obtain the final catalog.

Description	Number of sources
- Total of sources extracted with BLOBCAT	200
Rejected BLOBCAT sources ^a	9
Extended sources	8
Manually added extended sources	4
Rejected BLOBCAT CRSs	2
Manually added CRSs	1
Number of total extended sources	12
Number of CRSs in the final catalog	182

^aWe interpreted these sources as parts of extended ones that are counted in the 4th row (see text).

Table 2: Extended sources in the M17 region from the final map.

ID #	α [^h ^m ^s] (J2000)	δ [^o ['] ^{''}] (J2000)	S_{peak} ($\mu\text{Jy beam}^{-1}$)	S_{int} (μJy)	Area (arcsec^2)
1	18 20 24.931	-16 11 28.29	560 \pm 30	101425 \pm 5433	40.3
2	18 20 29.950	-16 12 46.44	117 \pm 19	12341 \pm 2004	20.5
3	18 20 26.264	-16 10 53.71	158 \pm 45	25439 \pm 7245	18.9
4	18 20 30.042	-16 08 40.72	76 \pm 15	12770 \pm 639	6.5
5	18 20 30.869	-16 08 48.88	160 \pm 15	9770 \pm 489	6.1
6	18 20 27.588	-16 08 31.24	103 \pm 18	8533 \pm 427	3.9
7	18 20 26.698	-16 13 14.56	244 \pm 25	9800 \pm 490	3.7
8	18 20 29.128	-16 08 58.76	251 \pm 16	4837 \pm 242	3.4
9	18 20 28.387	-16 11 19.52	81 \pm 10	2448 \pm 123	2.2
10	18 20 30.008	-16 11 01.08	57 \pm 7	887 \pm 109	2.1
11	18 20 26.736	-16 07 21.72	309 \pm 43	1707 \pm 237	0.5
12	18 20 26.813	-16 07 30.76	231 \pm 37	1903 \pm 304	0.4

Table 3: Distances of the Gaia counterparts of the CRSs

ID #	Parallax (mas)	Distance (kpc)
6	0.57 ± 0.32	1.75 ± 0.98
8	1.01 ± 0.19	0.99 ± 0.19
27	0.92 ± 0.21	1.09 ± 0.25
29	0.63 ± 0.10	1.59 ± 0.25
40	0.72 ± 0.12	1.39 ± 0.23
46	0.70 ± 0.24	1.43 ± 0.49
59	0.61 ± 0.16	1.64 ± 0.43
110	0.77 ± 0.155	1.30 ± 0.26
124	0.96 ± 0.55	1.04 ± 0.60
128	0.90 ± 0.15	1.11 ± 0.19
163	0.52 ± 0.11	1.92 ± 0.40
170	0.84 ± 0.20	1.19 ± 0.28

4.2. Rapid time variability

We constructed maps for the data corresponding to different observing days (May 3, May 4 and May 8) to search for rapid variability in the CRSs. We applied BLOBCAT to each map using a signal to noise ratio of 3σ because the individual maps are noisier than the map produced from the complete uv -data set.

The remaining faintest CRSs that BLOBCAT did not detect on single-day maps were measured using the task IMFIT. Then, we compared the fluxes of the CRSs between all the possible combinations of pairs of days by using the relation $V = (|S_{\text{day1}} - S_{\text{day2}}| \times 100) / S_{\text{max}}$, where S_{day1} and S_{day2} are the integrated fluxes on different days, and S_{max} is the larger of the two flux densities. We considered *highly variable sources* those with $V \geq 50\%$ (e.g., Dzib et al. 2013a), considering that the average variability of sources that are not highly variable is 30%. Table 5 shows a total of 72 CRSs with rapid high variability, around 40% of our catalog. Note that this fraction is a lower limit because some sources determined as non variable may be highly variable but be caught at an epoch in which their emission is steady. Assuming that our CRSs are YSOs, this lower limit is consistent with the result found in other regions (Dzib et al. 2013a, 2015; Ortiz-León et al. 2015a). The error in V was determined following standard error propagation theory. In Figure 2 we show an example of two CRSs close to each other that present rapid

Table 4: Spectral indices of the CRSs^a

ID #	S_{9GHz} (μJy)	S_{11GHz} (μJy)	Spectral Index
22	92486 ± 4626	111808 ± 5591	0.9 ± 0.3
30	867 ± 48	573 ± 31	-2.1 ± 0.4
31	405 ± 29	499 ± 27	1.0 ± 0.5
32	949 ± 55	791 ± 44	-0.9 ± 0.4
38	291 ± 21	222 ± 14	-1.4 ± 0.5
43	1526 ± 80	1814 ± 93	0.9 ± 0.4
47	254 ± 18	183 ± 11	-1.6 ± 0.5
69	656 ± 34	648 ± 33	-0.1 ± 0.4
79	885 ± 45	841 ± 43	-0.3 ± 0.4
84	250 ± 17	191 ± 12	-1.3 ± 0.5
86	519 ± 30	623 ± 34	0.9 ± 0.4
94	632 ± 33	581 ± 30	-0.4 ± 0.3
99	439 ± 24	395 ± 21	-0.5 ± 0.4
105	241 ± 16	186 ± 11	-1.3 ± 0.4
108	304 ± 19	208 ± 12	-1.9 ± 0.4
110	194 ± 14	138 ± 9	-1.7 ± 0.5
115	691 ± 36	701 ± 36	0.1 ± 0.4
120	785 ± 41	770 ± 39	-0.1 ± 0.4
151	692 ± 38	610 ± 33	-0.6 ± 0.4
152	893 ± 46	564 ± 29	-2.3 ± 0.4
159	369 ± 21	317 ± 17	-0.8 ± 0.4
161	164 ± 12	160 ± 10	-0.1 ± 0.5

^aWe only report sources with spectral index errors smaller than or equal to 0.5.

variability. The southern source decreases in luminosity in the lapse of a few days while the northern source exhibits the opposite behavior.

4.3. Polarization

We searched for circular polarization, which is indicative of gyrosynchrotron emission. To this end we used the CASA task CLEAN to map the Stokes V parameter. The rms noise was $4 \mu\text{Jy beam}^{-1}$ in the central region. Stokes V and I are measures of the circular polarization and total intensity (i.e. final map of Sect 2), respectively, of the radiation, where the V/I flux ration gives the degree of circular polarization. The polarization was considered significant only when the sources are close to the phase center ($< 1'$; sources more distant from the phase center suffer from the 'beam squint' effect that produces spurious circular polarization) and the flux density ratio ($S_{\text{peakV}} \times 100/S_{\text{peakI}}$) is greater than 3%, where S_{peakV} is the peak flux density from the Stokes V map and S_{peakI} is the peak flux density obtained in the Stokes I map. Table 6 shows S_{peakV} and S_{peakI} of the CRSs that fulfill these criteria and their corresponding flux density ratio. The error in the flux density ratio was determined following standard error propagation theory.

5. Discussion

The extraordinary large number of radio sources found in M 17 is possibly related with the hundreds of sources reported in previous surveys at other wavelengths (e.g., 771 X-ray sources with stellar counterparts and 96 candidate YSOs: Broos et al. 2007; Povich et al. 2009), as suggested by the counterparts reported in Sect. 3.4. As pointed out by RGM2012, their detected radio sources probably correspond to the same class of objects detected at other wavelengths and any lack of counterparts is caused by heavy extinction. In order to confirm the same trend in our CRSs, in Sect. 4 we explored some source properties, from which we attempt to unveil their emission mechanism. These properties will be discussed in this section and compared, when possible, to what is found for other regions.

In Fig. 3 we plot the spectral index vs. flux density for our brighter CRSs. Other than the predominance of negative spectral indices highlighted

in the previous sections, there are no significant trends in the diagram.

Given the deeper detection level achieved by Forbrich et al. (2016) in Orion, a significant trend was revealed, where the brighter sources in Orion (at least a few mJy) have positive spectral indices, while the sources with negative spectral indices are significantly weaker. This behavior is a consequence of the smaller emitting region of non-thermal emission in YSOs, usually limited to the stellar corona. At the same time, this implies that non-thermal emission associated to stellar objects usually appears point-like. While the presence of thermal sources of a few mJy in Orion is consistent with the 1.7 mJy source in M17 seen in the diagram (scaled by distance), our detection limit prevents us from searching for the aforementioned trend for fainter sources. However, while the highly variable CRSs corresponds to only 10% of the CRSs plotted in Figure 3, Table 6 shows that the fraction of highly variable CRSs represents 40% of our catalog, indicating that most of the highly variable CRSs are faint objects. Although variability is likely associated to non-thermal emission, additional factors are ususally required. If we assume that the trend of Forbrich et al. (2016) also applies to the sources of M17, then variability could be tied to non-thermal emission, at least for a substantial part of our CRSs (most of which do not appear in the graph).

Gyrosynchrotron radiation from stellar coronae is a common type of point-like, non-thermal emission found in regions of young stellar objects. In the case of gyrosynchrotron emission associated with low-mass stars, electrons accelerated during magnetic reconnection events are responsible both for the radio emission when they propagate in the stellar magnetic field, and the X-ray emission through their heating of the coronal gas (Benz & Güdel 2010). This type of emission can present variability and also shows a significant degree of circular polarization. Therefore, from the total catalog of CRSs, we identify polarized and variable sources as likely gyrosynchrotron candidates (e.g., Dulk 1985; Güdel et al. 2002; Dzib et al. 2013a, 2015; Ortiz-León et al. 2015a, hereafter referred to as Gy-CRS). We consider polarization and variability as complementary since some CRSs might be variable but present flux density stability during the short periods covered by our observations.

Table 5: Rapid highly variable sources

ID	<i>May</i> 3 – 4	<i>May</i> 4 – 8	<i>May</i> 3 – 8	ID	<i>May</i> 3 – 4	<i>May</i> 4 – 8	<i>May</i> 3 – 8
#	%	%	%	#	%	%	%
2	19 ± 4	55 ± 12	44 ± 9	83	13 ± 2	64 ± 9	58 ± 6
3	40 ± 10	75 ± 15	59 ± 14	84	41 ± 4	42 ± 5	66 ± 7
4	26 ± 6	59 ± 11	70 ± 17	93	0 ± 0	75 ± 26	75 ± 16
6	63 ± 18	54 ± 17	19 ± 5	96	≥ 14 ± 6	≥ 50 ± 18	57 ± 15
9	≥ 75 ± 26	≥ 88 ± 31	52 ± 8	97	≥ 54 ± 24	32 ± 10	≥ 68 ± 25
11	54 ± 9	11 ± 3	49 ± 11	101	35 ± 9	≥ 64 ± 25	≥ 44 ± 17
12	21 ± 4	41 ± 9	53 ± 10	104	≥ 24 ± 10	≥ 38 ± 14	53 ± 16
14	17 ± 2	60 ± 11	67 ± 11	106	64 ± 23	≥ 61 ± 24	≥ 10 ± 4
15	38 ± 10	≥ 62 ± 25	≥ 77 ± 27	111	≥ 59 ± 26	34 ± 11	≥ 73 ± 26
16	≥ 90 ± 32	27 ± 4	≥ 93 ± 32	114	≥ 17 ± 7	≥ 55 ± 19	62 ± 16
19	52 ± 14	45 ± 8	14 ± 3	117	≥ 43 ± 20	≥ 75 ± 26	≥ 86 ± 29
21	8 ± 2	84 ± 15	82 ± 12	123	6 ± 1	69 ± 16	67 ± 10
23	30 ± 5	≥ 77 ± 28	≥ 84 ± 29	124	9 ± 3	50 ± 23	54 ± 22
24	44 ± 4	66 ± 6	39 ± 3	125	7 ± 2	66 ± 17	63 ± 11
25	26 ± 3	74 ± 15	65 ± 13	127	3 ± 1	62 ± 10	63 ± 8
26	23 ± 8	≥ 41 ± 18	≥ 55 ± 21	131	88 ± 15	65 ± 7	66 ± 12
27	≥ 88 ± 33	39 ± 10	≥ 81 ± 32	136	≥ 92 ± 32	69 ± 11	≥ 76 ± 27
32	7 ± 1	50 ± 4	54 ± 5	139	35 ± 17	57 ± 23	72 ± 25
35	8 ± 2	77 ± 21	75 ± 15	144	≥ 43 ± 20	≥ 16 ± 6	≥ 52 ± 20
36	63 ± 18	≥ 47 ± 20	≥ 81 ± 28	146	49 ± 19	17 ± 5	58 ± 20
40	≥ 7 ± 3	≥ 90 ± 30	91 ± 22	152	3 ± 0.2	53 ± 4	52 ± 4
42	22 ± 6	≥ 61 ± 24	≥ 50 ± 18	158	≥ 17 ± 7	≥ 84 ± 28	86 ± 23
46	37 ± 13	≥ 32 ± 15	≥ 57 ± 20	162	17 ± 7	68 ± 25	61 ± 13
52	50 ± 15	24 ± 6	62 ± 18	163	66 ± 13	23 ± 4	55 ± 11
54	7 ± 2	≥ 52 ± 22	≥ 55 ± 20	164	33 ± 12	69 ± 20	79 ± 22
56	34 ± 16	25 ± 11	51 ± 18	167	30 ± 9	76 ± 19	66 ± 17
57	≥ 10 ± 4	≥ 58 ± 21	62 ± 16	170	36 ± 9	24 ± 7	52 ± 10
61	27 ± 13	48 ± 20	62 ± 18	171	≥ 60 ± 40	≥ 77 ± 26	91 ± 54
62	33 ± 11	37 ± 11	57 ± 15	173	0 ± 0	88 ± 11	88 ± 16
65	15 ± 5	≥ 55 ± 23	≥ 46 ± 17	174	17 ± 3	52 ± 10	42 ± 5
66	61 ± 18	45 ± 9	78 ± 20	175	≥ 47 ± 16	≥ 83 ± 29	68 ± 10
71	52 ± 8	85 ± 10	93 ± 12	177	≥ 41 ± 14	≥ 51 ± 18	16 ± 3
73	5 ± 2	65 ± 18	63 ± 11	178	≥ 87 ± 31	70 ± 15	≥ 56 ± 21
78	17 ± 4	≥ 61 ± 24	≥ 53 ± 19	179	12 ± 6	53 ± 28	59 ± 13
82	≥ 51 ± 22	56 ± 17	≥ 78 ± 28	182	53 ± 23	16 ± 7	44 ± 10

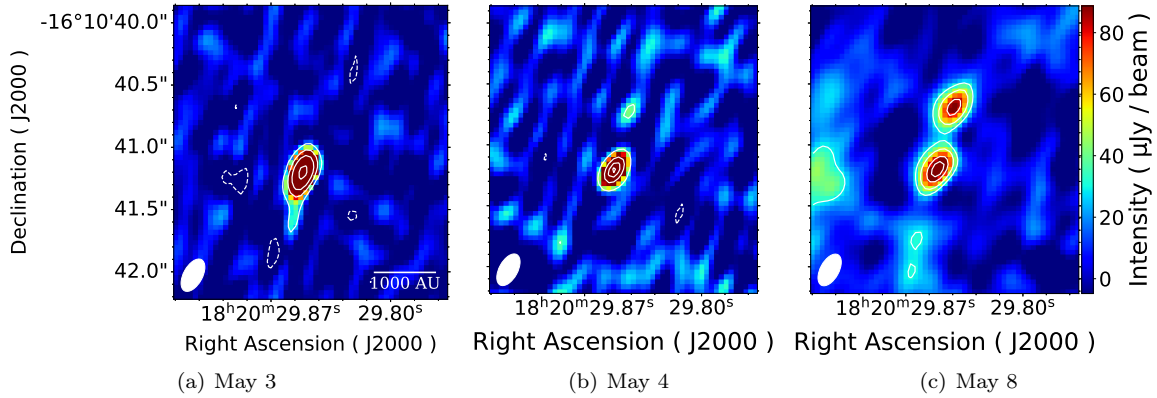


Fig. 2.— Detailed view of rapid variability on two sources close to each other. The northern source is the number 82 and the southern source is the number 84. The color scale is the same in the three panels. In (a) we show the map on May 3. Contours are $-3, 3, 10, 20$ and 40 times $8 \mu\text{Jy beam}^{-1}$. In (b) we show the map on May 4. Contours are $-3, 3, 10, 15$ and 18 times $12 \mu\text{Jy beam}^{-1}$. In (c) we show the map on May 8. Contours are $-3, 3, 10, 15$ and 18 times $12 \mu\text{Jy beam}^{-1}$.

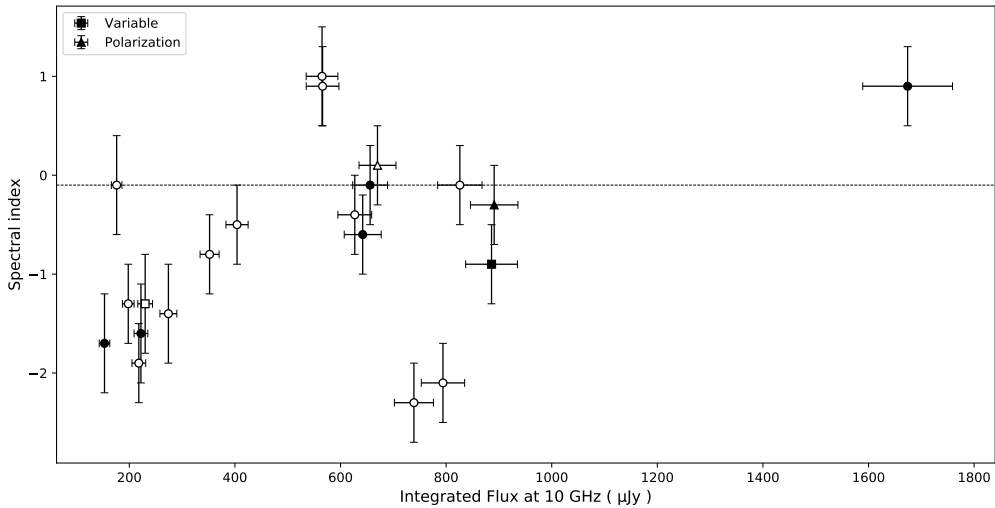


Fig. 3.— Spectral index against integrated flux density at 10 GHz of the brightest CRSs. Squares are the highly variable sources. Triangles are the sources with polarization. The filled symbols are those with X-ray counterpart and the unfilled are the sources without an X-ray counterpart. The UC1 source is not included in the plot. The dashed line marks a spectral index of -0.1 .

The rest of the CRSs cannot be uniquely categorized and we leave their nature as undetermined (hereafter referred to as Und-CRS). A small fraction of Und-CRS might be thermal emitters and they could be small trapped HCHII regions or proplyds. Moreover, some Und-CRS have IR counterparts that could indicate the presence of heated dust. The typical fluxes detected by us

($< 1 \text{ mJy}$) are similar to those of proplyds detected in Orion (Zapata et al. 2004) scaled to the M17 distance and, thus, we favor the proplyd scenario. Other Und-CRS could be non-thermal emitters that present low or no variability (e.g., collision wind region between massive stars where electrons are highly accelerated). Observations at higher frequencies with higher angular resolution

Table 6: Circularly polarized sources.

ID #	S_{peakV} ($\mu\text{Jy bm}^{-1}$)	S_{peakI} ($\mu\text{Jy bm}^{-1}$)	Flux density ratio %
56	17 ± 3	42 ± 6	40 ± 9
62	-16 ± 4	34 ± 6	47 ± 5
95	17 ± 4	79 ± 7	21 ± 5
113	-14 ± 5	46 ± 6	30 ± 12
122	16 ± 5	61 ± 6	26 ± 9

are needed to explore the nature of Und-CRS.

5.1. The X-ray–Radio connection

As we mentioned earlier, it is thought that the X-ray and radio emissions in stellar coronas are both caused by electrons accelerated during magnetic reconnection events. The electrons accelerated during these events generate the radio emission via the gyro-synchrotron mechanism, but they also heat the corona to temperatures sufficient to produce thermal bremsstrahlung X-ray emission (Dulk 1985; Feigelson & Montmerle 1999; Güdel et al. 2002). This correlation between radio and X-ray emission was first investigated empirically by Güdel & Benz (1993) and Benz & Güdel (1994) for a population of coronally active stars and this relation was found:

$$\frac{L_X}{L_R} = \kappa 10^{15.5 \pm 0.5} \quad (2)$$

with $\kappa \leq 1$ accounting for different types of stars. For instance, several works show that κ is significantly lower than 1 for YSOs (Gagné et al. 2004; Dzib et al. 2013a, 2015).

From our catalog, 24 of 182 CRSs have X-ray counterparts with measured luminosities reported in Broos et al. (2007), and some of them are absorption corrected. They followed a similar methodology as that in Feigelson et al. (2002): wide band fluxes were obtained and converted to total-band luminosities (0.5–8 keV) by fitting a thermal plasma model to the data under the maximum likelihood method. The fit also gives the absorbing column of interstellar material and, thus, corrected luminosities by absorption can also be obtained. When the fit yielded unrealistic physical parameters, Broos et al. employed a power-law model to fit the data. Besides, some corrected luminosities measured only the hard X ray

band (2–8 keV) and hence are meaningless because they correspond to highly obscured sources. Thus, the absorption-corrected luminosities are omitted for these sources and only their observed luminosities are reported. The X-ray luminosities and our derived radio luminosities for CRSs in M17 are shown in Figure 4. In this plot, we excluded those Gaia counterparts not belonging to the region (i.e., foreground sources). A linear least squares fit to the 21 remaining data points shown in Figure 4 gives:

$$\log L_X = (26.6 \pm 5.7) + (0.26 \pm 0.32) \log L_R$$

with a correlation coefficient (R) of 0.17. Since this coefficient has a low value, we conclude that the radio and X-ray luminosities are not correlated and, thus, do not follow a Güdel-Benz relation, where a slope consistent with 1 is expected. Note that, in general, our data are underluminous in X-ray emission. Lower X-ray luminosities than those predicted by the Güdel-Benz relation are also found in other star forming regions (Kounkel et al. 2014; Dzib et al. 2013a; Ortiz-León et al. 2015a; Dzib et al. 2015; Forbrich et al. 2016), meaning that we are likely picking up objects of the same nature. Also, Gy-CRS and Und-CRS follow the same behavior and there is no segregation between them.

The lack of correlation between X-ray and radio data can be due to several reasons. First, our data sample is contaminated by a number of possible thermal sources because points from the undetermined category (black dots) are dominant in the graph, while the Güdel-Benz relation only applies for non-thermal sources. Second, our sample is small and CRSs with luminosities below $\log(L_R) \sim 17.0 \text{ erg s}^{-1}\text{Hz}^{-1}$ are not detected, perhaps due to a lack of completeness, adding uncertainty in the slope determination. This is not surprising since M17 is further away than other nearby regions observed in similar studies (Dzib et al. 2013a; Ortiz-León et al. 2015a) and suggests that the faintest objects of our region remain undetected by our observations.

As discussed by Forbrich et al. (2016), a similar trend is observed for the 250 ONC sources with both X-ray and radio emission. If we fit their respective luminosities we obtain:

$$\log L_X = (24.1 \pm 1.6) + (0.37 \pm 0.10) \log L_R$$

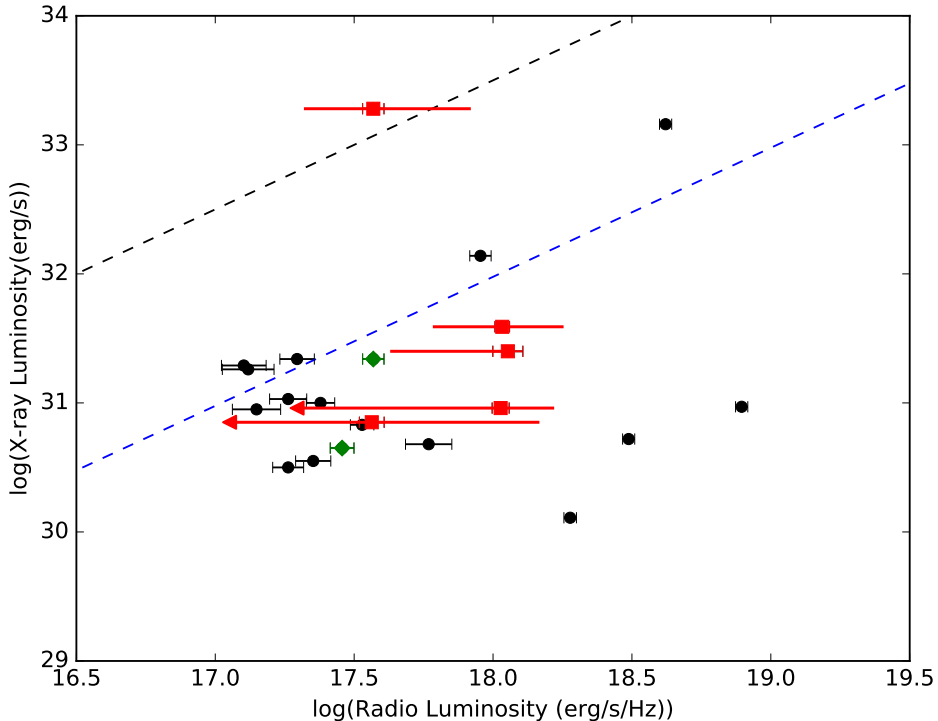


Fig. 4.— X-ray luminosity vs. Radio luminosity at 10 GHz of the CRSs in M17. Black dots represents the Und-CRS, green diamonds are sources with circular polarization and red squares are variable sources (these two types of sources are Gy-CRS), with the horizontal red bars representing the range of variability between our observing epochs. If the variable source is undetected in one or more epochs, we report upper limits as arrows at the lower end of the range. The black solid and blue dashed lines represent the Güdel-Benz relation with $\kappa = 1$ and 0.03 , respectively, the latter employed by Dzib et al. (2013a) to match radio and X-ray luminosities of YSOs.

again suggesting that the X-ray and radio luminosities are poorly correlated, if at all ($R=0.23$). This is not unexpected since a large fraction of the radio sources in the ONC are thermal and their intensity is unrelated to the mildly relativistic electrons that produce the X-ray and gyrosynchrotron emission in active stars (Güdel & Benz 1993). If, in contrast, for Orion we consider only the 82 sources with X-ray emission that are also VLBI sources (Forbrich et al. 2021; Dzib et al. 2021) and whose emission is thus clearly non-thermal¹, a

¹We consider a VLBI source as a non-thermal emitter since the VLBI technique filters out the thermal emission leaving only the most compact emission with high brightness temperatures ($> 10^6$ K), a strong indicator of non-thermal

clear correlation is obtained. These data are fitted by:

$$\log L_X = (17.1 \pm 2.4) + (0.81 \pm 0.14) \log L_R.$$

consistent with a linear fit ($R=0.53$). The data and fit are shown in Figure 5. The obtained fit for this case is also about an order of magnitude lower in L_X than the original Güdel-Benz relation. This result confirms the notion that the radio emission is probably produced by gyrosynchrotron radiation from the same mildly relativistic electrons that are responsible for the X-ray emission. Unfortunately, the same test for the M17 data yields

emission associated to young stars (e.g., Feigelson & Montmerle 1999).

unreliable results because we have only 8 sources with X-ray emission and non-thermal characteristics in the radio. Nevertheless, we have plotted this handful of sources in Figure 5 to show that they fall near the high-brightness portion of the Orion data. We speculate that more sensitive observations of M17 will reveal a similar population of related radio - X-ray sources. As discussed below, for a given radio luminosity M17 has about three times the number of sources of Orion. In practice, however, given its larger distance it will be very difficult to obtain an M17 survey with similar luminosity limits as those obtained for Orion.

5.2. The luminosity function

The high number of detected CRSs towards M17 (182 CRSs) makes this region the second richest in radio source detections after the ONC (556 CRSs), and followed by NGC 6334 (83 CRSs). Thus, a comparison between these regions is tempting. In Figure 6 we show histograms for the radio luminosity distribution (number of CRSs per logarithmic luminosity interval) of the three regions of star formation considered here. Unfortunately, because of their larger distances, we are severely limited in the dynamic range for M17 and NGC 6334D-F due to incompleteness, and a comparison can be made only for the two bins of higher luminosity.

M17 has about three times more sources at a given radio luminosity than the other two regions. This result is probably related with the significantly higher global luminosity (stars plus dust) that M17 has over the two other regions (Johnson 1973). We also conclude that the negative slope between these two luminosity bins is, within error, the same for all three regions. We find that, approximately, the number of sources drops inversely (in a linear relation) with their radio luminosity.

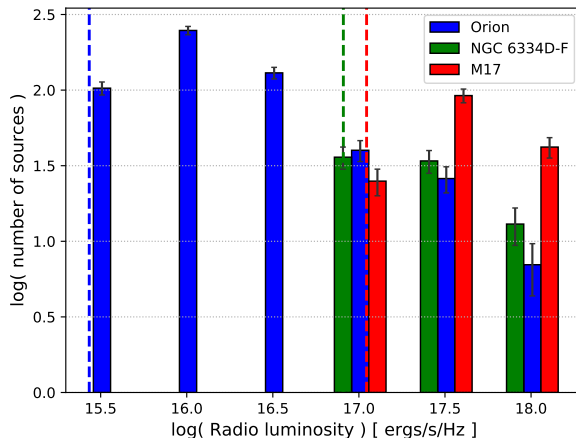


Fig. 6.— Radio luminosity distribution of M17 (red bars, this work), NGC 6334D-F (green bars, Medina et al. 2018) and Orion (blue bars, Forbrich et al. 2016). The error bars are the uncertainty assuming that the number of sources in each luminosity bin follows a Poisson distribution. The vertical dashed lines indicate the adopted detection limit for each region according to the respective color. Note that the position of these lines makes the $\log(\text{Radio luminosity}) = 17.0$ erg/s/Hz bins incomplete for M17 and NGC 6334D-F. The width of each bin is 0.5 dex.

5.3. Age and spatial distribution of the CRSs

The VLA observations from the Gould’s Belt Very Large Array Survey studied the radio emission from hundred of YSOs in nearby (< 500 pc) star-forming regions (Dzib et al. 2013b, 2015; Kounkel et al. 2014; Ortiz-León et al. 2015b; Pech et al. 2016). The results have shown that the properties of the radio emission (variability, spectral index, and circular polarization) change with the infrared classification of YSOs. Class 0, and Class I young stars are mostly associated with thermal free-free radio emission, Class III with gyrosynchrotron radio emission and Class II is an intermediate case. However, some Class I YSOs have been confirmed to be gyrosynchrotron radio emitters (e.g., Dzib et al. 2010). Thus, gyrosynchrotron sources usually correspond to relatively evolved young stars with clean surroundings and their photosphere visible at optical wavelengths

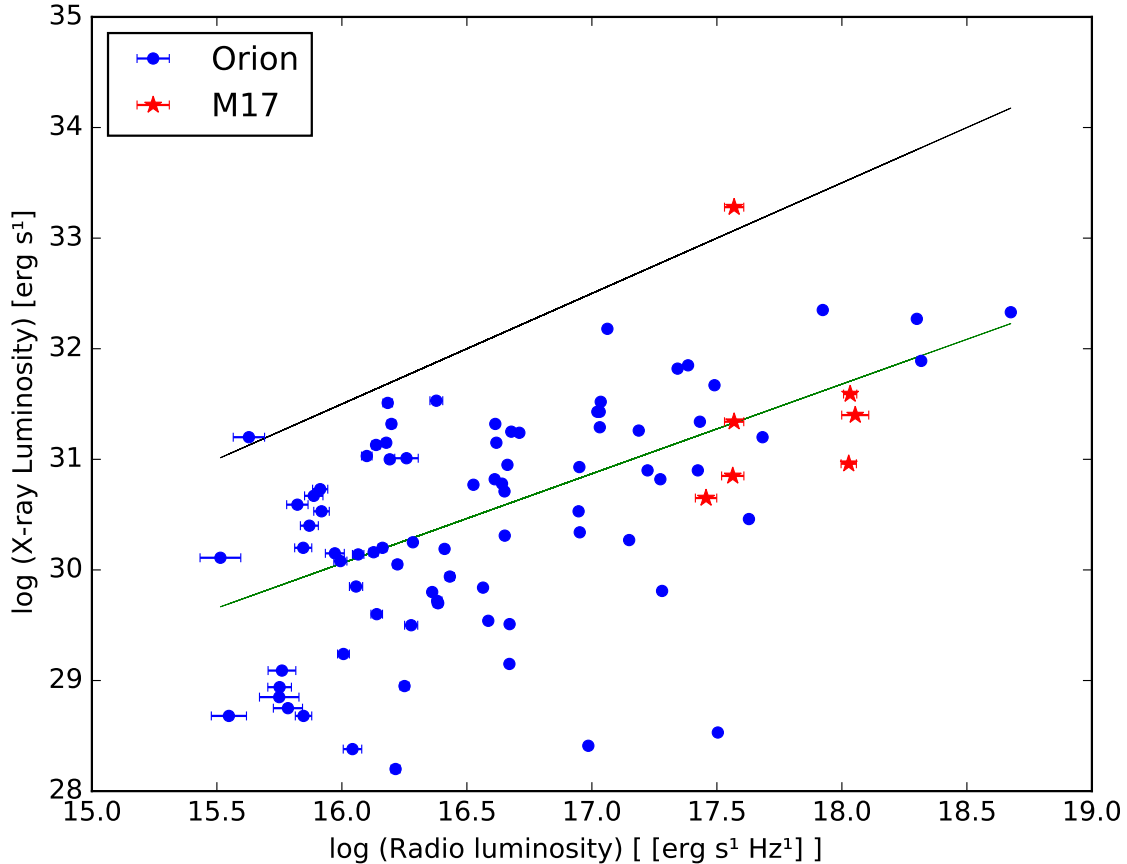


Fig. 5.— X-ray luminosities as a function of radio luminosity. The points mark the position of the 82 X-ray sources that are also detected with VLBI techniques (blue dots). The red stars are data points of the M17 region with X-ray emission and non-thermal characteristics in the radio. The green line is the fit discussed in the text. The black line is the original Güdel-Benz relation.

(Class III YSOs). On the other hand, thermal sources are likely younger objects still embedded in large envelopes of circumstellar material that are strongly accreting and at the same time producing jets whose free-free emission is dominant. The large number of gy-CRSs detected by us (36% of the total CRSs, twice the VLBI sources found in Orion: $\sim 20\%$ of the total radio sources) suggests the existence of an important evolved population of young objects in the M17 region. The Und-CRS, on the other hand, probably include young thermal sources.

In the past, objects of different ages have been

found in M17. For instance, Nielbock et al. (2001) analyzed 22 compact NIR sources and deduced that most of them are massive stars of Class I type, indicating that these objects formed very recently. In contrast, Broos et al. (2007) analyzed 138 stars and found that only 12% are Class I and II, indicating a predominance of older Class II and III sources toward M17. Our results agree with the scenario of an age dispersion for the objects in M17 and suggest that the region has been forming stars at least ten million years (i.e. the age of Class III objects).

In Figure 7 we show the distribution of CRSs in

the M 17 region highlighting the Gy-CRSs in pink. The distribution of the two populations looks centrally peaked and smoothly fades in the outskirts of the map. Thus, to analyze the spatial distribution of radio sources in M 17 we have fitted the data to a Gaussian ellipsoid following Rodriguez-Gomez et al. (2019). In Table 7 we present the parameters (centroid, major and minor axis and position angle of the major axis) for Gaussian ellipsoids fitted to the three populations of radio sources in M 17 and in Orion, aiming to compare any segregation between populations in both regions. Note that the axes of the distributions are significantly smaller than the primary beam size.

We conclude that for the case of Orion all three populations have parameters that overlap to within one-sigma. Perhaps this result is related to the lack of expansion or contraction motions found by Dzib et al. (2017) from observations of 88 young stars with compact radio emission. It also suggests that, despite their age, the stars will remain similarly distributed.

For M 17, the centroids are consistent within the noise and fall within a few arcsec of the positions of the massive binary system formed by CEN 1a and CEN 1b. Also the position angles are consistent within one-sigma. However, the major and minor axes of the non-thermal population seem to be about 20 percent larger than those of the other two populations, and significantly smaller than the primary beam size. The rough coincidence of the centroids of all three distributions in M 17 with CEN 1 is consistent with a scenario where the potential well of the cloud centers on this massive binary star, and most of the objects (including the most massive) are formed around this position. Besides, the larger dispersion of the Gy-CRS is marginal and a direct measurement of their proper motions is required to provide a conclusive statement.

We finally note that the radio population in M 17 is not only about three times more abundant (a result inferred from the comparison of the most luminous sources) than in Orion, but also that it is more extended spatially. Correcting for the distance (388 ± 5 pc, Kounkel et al. 2017), the major axis of the distribution of all sources in Orion corresponds to 0.17 pc, while it is 0.84 pc for the case of M 17.

5.4. The Hyper-Compact HII region UC1 and the Arc structure

In Figure 8 we focus on the X band emission at the western part of the cloud. The left panel of the figure shows the arc-shaped structure found previously by Felli et al. (1980) and discussed by Felli et al. (1984) and Johnson et al. (1998). This structure is identified as the ionizing front of the central HII region of M 17. For the whole arc-like structure, we measure a flux density of 0.1 Jy and a bounding box of $\sim 5 \times 30$ arcsec. These values are significantly lower than those measured by Felli et al. (1984) because our data suffer from severe spatial filtering.

Near the focus of the arc morphology, Felli et al. (1980) found a compact thermal radio source they named UC1 and which they categorized as an UCHII region. Felli et al. (1984) determined a size (~ 0.004 pc) and spectral index (~ 1) that RGM2012 found more typical of an HCHII region. Our measured flux density value at 10 GHz, 98 ± 5 mJy, is roughly consistent with the results of the spectral analysis of RGM2012. However, RGM2012 showed that the spectral index derived for UC1 actually results from averaging a gradient along the cometary morphology highlighted in the right panel of Figure 8 (countours). The gradient on the spectral index is likely a consequence of a gas density gradient in the source, being maximum at the tip of the cometary morphology at the south-east part of the source (i.e., implying emission measures of at least $\sim 10^9$ cm⁻⁶ pc).

We obtained archival ALMA band 6 data centered on UC1 in order to assess the scenario of RGM2012 described above (project 2015.1.01163). In agreement with this scheme, the mm emission integrated over the entire band (1.875 GHz) shows a bow-like structure oriented toward the SE, where high densities, either of dust or ionized material are expected to be found. In addition, a bright central source possibly associated with the stellar object of UC1 is also revealed in the mm map. The total integrated flux density of the mm emission centered at 228 GHz is about 125 mJy, 7 mJy of which come from this central source. The deconvolved size of the latter is $(30 \pm 10$ mas) \times $(22 \pm 17$ mas) (P.A. of $70^\circ \pm 50^\circ$) that at the distance of M 17 corresponds to $\sim 60 \times 40$ AU. If this mm emission comes from a protostellar disk, its de-

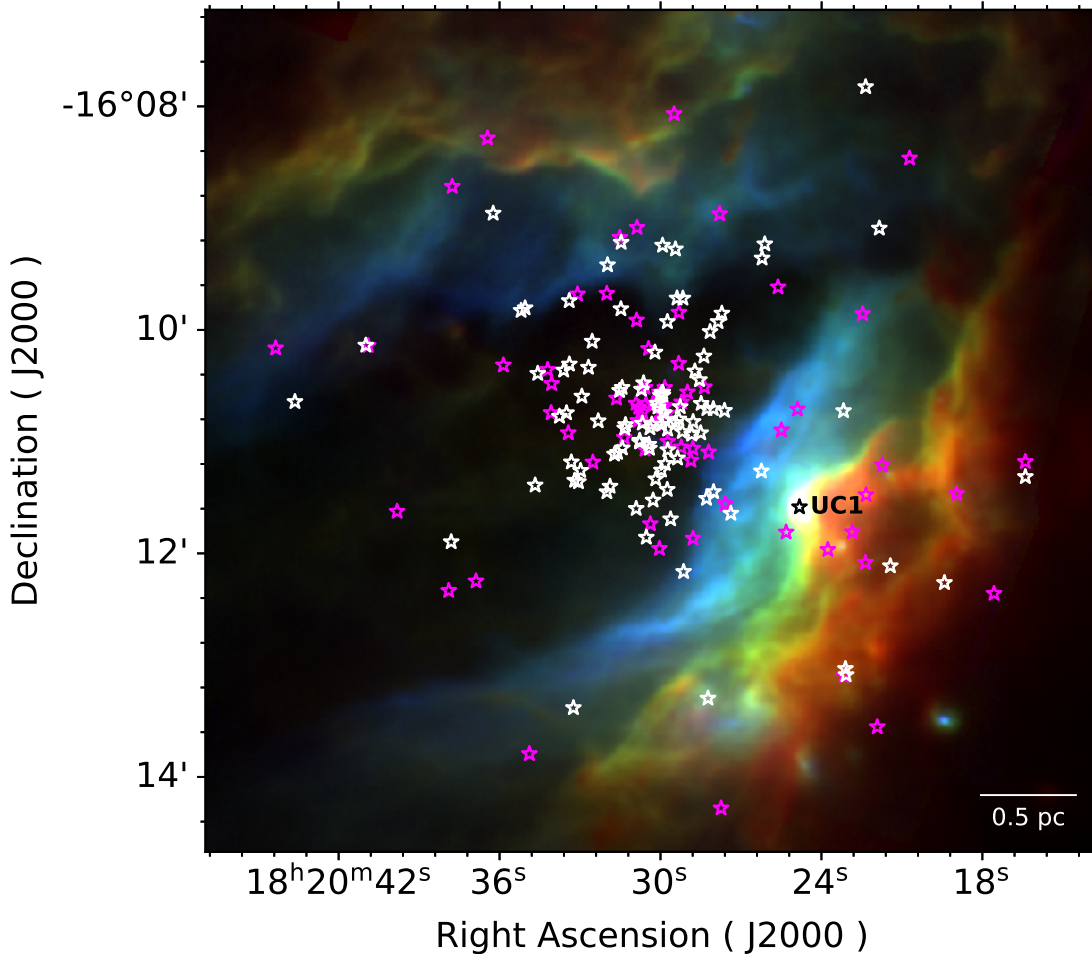


Fig. 7.— RGB image toward M17 of $\sim 7' \times 7'$ of field. Blue corresponds to the SOFIA-FORCAST $20 \mu\text{m}$ image, green is the SOFIA $37 \mu\text{m}$ image and red is the Herschel $70 \mu\text{m}$ image. Pink stars represents the position of the Gy-CRS and white stars are the Und-CRS. The black star shows the UC1 position. The SOFIA images are taken from Lim et al. (2020).

rived size is significantly lower than the sizes inferred for disks of other massive stars (~ 300 AU and a few hundreds of mJy at similar wavelengths, Lugo et al. 2004; Girart et al. 2018). A possibility is that the disk is being ablated by the energetic radiation of the protostellar object exciting UC1, although we cannot discard alternative scenarios involving other elements than the presence of a disk.

Exploring UC1 at IR wavelengths, Nielbock et al. (2007) found hints of a disk-like structure in absorption across UC1, which was interpreted as a cool disk of 1000 AU in size. This size is more

than an order of magnitude larger than the size of the central peak of the ALMA image. The fact that more extended material from this cool disk is not detected at the frequency of the ALMA observations suggests that it corresponds to a different structure, perhaps associated to the molecular part of the M17 region. The potential role of disks around massive stars, in particular in their early stages (i.e., HCHII region) is presently unclear and their firm detection would have important implications on the paradigm of their formation and deserves further investigation.

Table 7: Statistical parameters of the spatial distribution of CRSs

CRS Type	Mean Position		Size		
	α (J2000)	δ (J2000)	Major Axis ($''$)	Minor Axis ($''$)	Position Angle (deg.)
M17					
All CRS	$18^{\text{h}}20^{\text{m}}29^{\text{s}}84 \pm 0^{\text{s}}33$	$-16^{\circ}10'47''9 \pm 4''5$	66.9 ± 3.8	55.2 ± 3.0	52.0 ± 12.6
Gy-CRS	$18^{\text{h}}20^{\text{m}}29^{\text{s}}54 \pm 0^{\text{s}}61$	$-16^{\circ}10'49''7 \pm 8''2$	79.2 ± 6.7	61.9 ± 5.2	53.6 ± 19.1
Und-CRS	$18^{\text{h}}20^{\text{m}}30^{\text{s}}04 \pm 0^{\text{s}}37$	$-16^{\circ}10'46''6 \pm 5''3$	56.6 ± 3.9	50.0 ± 3.5	47.8 ± 16.3
Orion Nebula Cluster					
All sources	$5^{\text{h}}35^{\text{m}}16^{\text{s}}36 \pm 0^{\text{s}}21$	$-5^{\circ}22'55''3 \pm 3''4$	87.1 ± 2.6	67.7 ± 2.0	-17.4 ± 7.1
VLBI radio sources ^a	$5^{\text{h}}35^{\text{m}}16^{\text{s}}45 \pm 0^{\text{s}}45$	$-5^{\circ}23'2''2 \pm 7''8$	90.0 ± 5.8	69.0 ± 4.4	-28.7 ± 15.1
non-VLBI radio sources ^b	$5^{\text{h}}35^{\text{m}}16^{\text{s}}34 \pm 0^{\text{s}}22$	$-5^{\circ}22'53''4 \pm 4''1$	86.4 ± 2.9	66.9 ± 2.3	-14.0 ± 8.0

^aForbrich et al. (2021) and Dzib et al. (2021)

^bForbrich et al. (2016)

6. Conclusions

We have carried out deep X band observations with the VLA operating in A configuration. After self-calibrating the obtained data of M17 and extracting radio sources by applying the BLOBCAT software on the resulting map, we cataloged them and inspected their basic emission properties. We reached the following conclusions:

1. We found a total of 194 radio sources in the M17 region, 12 of them extended and 182 compact. This catalog constitutes the most complete catalog of radio sources known of M17. After Orion, M17 becomes the second richest region in radio source detection to our knowledge.
2. The inspection of the properties of our radio sources reveals a population (about 40% of our catalog) of objects emitting non-thermal radiation. These are probably low-mass stars with coronal gyrosynchrotron emission, given their observed variability and polarization.
3. In X-ray emission, these non-thermal radio sources are underluminous with respect to the Güdel Benz relation, but a reasonable correlation of their radio and X-ray emission is still found, provided that only sources with evident non thermal nature are selected from Orion and M17. This suggests that radio and X-ray emission are both caused the

same underlying process, presumably magnetic reconnection in the stellar coronae.

4. The luminosity function of the M17 radio sources shows a decreasing trend with luminosity (i.e. weak sources are more abundant than bright ones). The same trend is observed for the radio sources of the Orion Nebula Cluster and NGC 6334D-F reported in other works, though there is an important lack of completeness for M17 and NGC 6334D-F that prevents us from exploring this similarity for the weakest sources. In any case, M17 has about three more times sources at any given radio luminosity than the other two regions perhaps due to its higher intrinsic luminosity.
5. The spatial distribution of sources in M17 is centrally peaked towards the position of the most massive stars (e.g., CEN 1) and fades radially and smoothly toward the outskirts of the region, with a dispersion that is marginally higher for non thermal sources. The same analysis carried out for the radio sources in the ONC shows no segregation between thermal and non thermal sources. The radio cluster in M17 is about 5 times larger than that in the ONC.
6. A previously known arc structure that has the HCHII region UC1 at its focus is also detected in our image. The cometary morphology of UC1 is highlighted in our data with a probable increase of density towards

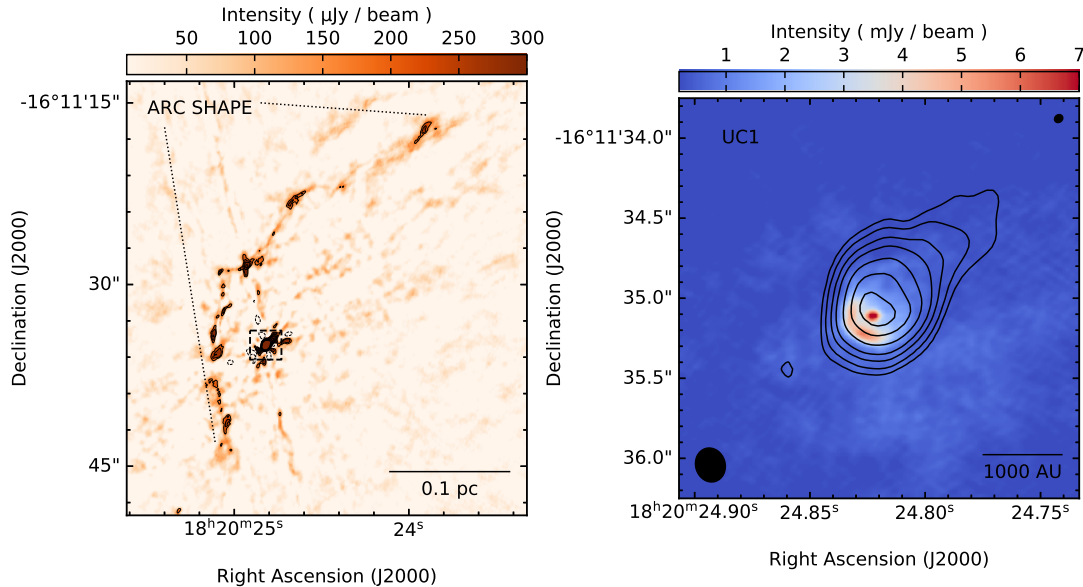


Fig. 8.— *Left Panel:* X band emission (color and contour scale) highlighting the arc shape structure (West part of the image). Contour levels are C times -2^0 , $2^{1/2}$, 2^1 , $2^{3/2}$, 2^2 , $2^{5/2}$, 2^3 , $2^{7/2}$ and 2^4 , where C is given by 2.5 times the rms noise measured over the region of the map shown in the panel ($70 \mu\text{Jy beam}^{-1}$). The beam size is the same as shown in Fig. 1. The dotted lines show the angular extend of the Arc shape. The dashed box represents the area shown enlarged in the right panel enclosing the UC1 source. *Right Panel:* Detail of the X band emission (contours) of UC1 superimposed on the ALMA 240 GHz continuum image (color scale). Note the compact ALMA source that we identify as a disk associated with the ionizing star of the region. Contours are 3, 6, 12, 20, 35, 53 and 68 times the rms noise of the region of the map around UC1 ($25 \mu\text{Jy beam}^{-1}$). The corresponding beams are shown in the bottom left corner (VLA) and in the top right corner (ALMA).

the ionization front traced by the arc. Exploring ALMA archival data at 1 mm, we found emission associated to the possible exciting source of UC1. If this emission comes from a protoplanetary disk, its size is considerably smaller than typical sizes inferred from disks around massive protostars.

Acknowledgements

V.Y. acknowledges the financial support of DAIP, UG, and MPIfR during the internship at the Max Planck Institute for Radioastronomy. V.Y. acknowledges the financial support of CONACyT, México. L.L. acknowledges the support of CONACyT-AEM grant 275201, CONACyT-CF grant 263356, and UNAM DGAPA/PAPIIT grants IN112417 and IN112820.

This research has made use of the NASA/IPAC Infrared Science Archive, which is funded by the National Aeronautics and Space Administration and operated by the California Institute of Technology. Counterparts to radio sources were found by using SIMBAD database.

Facilities: This work makes use of the Spitzer, 2MASS, Gaia, Vary Large Array (VLA), and Atacama Large Millimeter Array (ALMA) telescopes. The VLA observations presented here were part of NRAO program 18A-002. The National Radio Astronomy Observatory is a facility of the National Science Foundation operated under cooperative agreement by Associated Universities, Inc. This paper makes use of the following ALMA data: ADS/JAO.ALMA#2015.1.01163. ALMA is a partnership of ESO (representing its member

states), NSF (USA) and NINS (Japan), together with NRC (Canada), MOST and ASIAA (Taiwan), and KASI (Republic of Korea), in cooperation with the Republic of Chile. The Joint ALMA Observatory is operated by ESO, AUI/NRAO and NAOJ.

REFERENCES

- Anglada, G., Rodríguez, L. F., & Carrasco-González, C. 2018, *A&A Rev.*, 26, 3
- Anglada, G., Villuendas, E., Estalella, R., Beltrán, M. T., Rodríguez, L. F., Torrelles, J. M., & Curiel, S. 1998, *AJ*, 116, 2953
- Avalos, M., Lizano, S., Franco-Hernández, R., Rodríguez, L. F., & Moran, J. M. 2009, *ApJ*, 690, 1084
- Beetz, M., Elsaesser, H., Weinberger, R., & Poulakos, C. 1976, *A&A*, 50, 41
- Benz, A. O. & Güdel, M. 1994, *A&A*, 285, 621
- . 2010, *ARA&A*, 48, 241
- Bertin, E. & Arnouts, S. 1996, *A&AS*, 117, 393
- Bihl, S., Johnston, K. G., Beuther, H., Anderson, L. D., Ott, J., Rugel, M., Bigiel, F., Brunthaler, A., Glover, S. C. O., Henning, T., Heyer, M. H., Klessen, R. S., Linz, H., Longmore, S. N., McClure-Griffiths, N. M., Menten, K. M., Plume, R., Schierhuber, T., Shanahan, R., Stil, J. M., Urquhart, J. S., & Walsh, A. J. 2016, *A&A*, 588, A97
- Blomme, R., Nazé, Y., Volpi, D., De Becker, M., Prinja, R. K., Pittard, J. M., Parkin, E. R., & Absil, O. 2013, *A&A*, 550, A90
- Broos, P. S., Feigelson, E. D., Townsley, L. K., Getman, K. V., Wang, J., Garmire, G. P., Jiang, Z., & Tsuboi, Y. 2007, *ApJS*, 169, 353
- Brunthaler, A., Menten, K. M., Dzib, S. A., Cotton, W. D., Wyrowski, F., Dokara, R., Gong, Y., Medina, S. N. X., Müller, P., Nguyen, H., Ortiz-León, G. N., Reich, W., Rugel, M. R., Urquhart, J. S., Winkel, B., Yang, A. Y., Beuther, H., Billington, S., Carrasco-Gonzalez, C., Csengeri, T., Murugesan, C., Pandian, J. D., & Roy, N. 2021, *A&A*, 651, A85
- Chini, R., Elsaesser, H., & Neckel, T. 1980, *A&A*, 91, 186
- Chini, R., Hoffmeister, V. H., Kämpgen, K., Kimeswenger, S., Nielbock, M., & Siebenmorgen, R. 2004, *A&A*, 427, 849
- Chini, R. & Kruegel, E. 1985, *A&A*, 146, 175
- Chini, R. & Wargau, W. F. 1998, *A&A*, 329, 161
- Churchwell, E., Felli, M., Wood, D. O. S., & Massi, M. 1987, *ApJ*, 321, 516
- Dougherty, S. M. & Williams, P. M. 2000, *MNRAS*, 319, 1005
- Dulk, G. A. 1985, *ARA&A*, 23, 169
- Dzib, S., Loinard, L., Mioduszewski, A. J., Boden, A. F., Rodríguez, L. F., & Torres, R. M. 2010, *ApJ*, 718, 610
- Dzib, S. A., Forbrich, J., Reid, M. J., & Menten, K. M. 2021, *ApJ*, 906, 24
- Dzib, S. A., Loinard, L., Mioduszewski, A. J., Rodríguez, L. F., Ortiz-León, G. N., Pech, G., Rivera, J. L., Torres, R. M., Boden, A. F., Hartmann, L., Evans, Neal J., I., Briceño, C., & Tobin, J. 2013a, *ApJ*, 775, 63
- Dzib, S. A., Loinard, L., Rodríguez, L. F., Gómez, L., Forbrich, J., Menten, K. M., Kounkel, M. A., Mioduszewski, A. J., Hartmann, L., Tobin, J. J., & Rivera, J. L. 2017, *ApJ*, 834, 139
- Dzib, S. A., Loinard, L., Rodríguez, L. F., Mioduszewski, A. J., Ortiz-León, G. N., Kounkel, M. A., Pech, G., Rivera, J. L., Torres, R. M., Boden, A. F., Hartmann, L., Evans, Neal J., I., Briceño, C., & Tobin, J. 2015, *ApJ*, 801, 91
- Dzib, S. A., Rodríguez-Garza, C. B., Rodríguez, L. F., Kurtz, S. E., Loinard, L., Zapata, L. A., & Lizano, S. 2013b, *ApJ*, 772, 151
- Elmegreen, B. G., Lada, C. J., & Dickinson, D. F. 1977, in *Bulletin of the American Astronomical Society*, Vol. 9, 588
- Feigelson, E. D., Broos, P., Gaffney, James A., I., Garmire, G., Hillenbrand, L. A., Pravdo, S. H., Townsley, L., & Tsuboi, Y. 2002, *ApJ*, 574, 258

- Feigelson, E. D. & Montmerle, T. 1999, *ARA&A*, 37, 363
- Felli, M., Johnston, K. J., & Churchwell, E. 1980, *ApJ*, 242, L157
- Felli, M., Massi, M., Staude, H. J., Reddmann, T., Eiroa, C., Hefele, H., Neckel, T., & Panagia, N. 1984, *A&A*, 135, 261
- Fleishman, G. D. & Melnikov, V. F. 2003, *ApJ*, 587, 823
- Forbrich, J., Dzib, S. A., Reid, M. J., & Menten, K. M. 2021, *ApJ*, 906, 23
- Forbrich, J., Rivilla, V. M., Menten, K. M., Reid, M. J., Chandler, C. J., Rau, U., Bhatnagar, S., Wolk, S. J., & Meingast, S. 2016, *ApJ*, 822, 93
- Gagné, M., Skinner, S. L., & Daniel, K. J. 2004, *ApJ*, 613, 393
- Garay, G., Moran, J. M., & Reid, M. J. 1987, *ApJ*, 314, 535
- Girart, J. M., Fernández-López, M., Li, Z.-Y., Yang, H., Estalella, R., Anglada, G., Añez-López, N., Busquet, G., Carrasco-González, C., Curiel, S., Galvan-Madrid, R., Gómez, J. F., de Gregorio-Monsalvo, I., Jiménez-Serra, I., Krasnopolsky, R., Martí, J., Osorio, M., Padovani, M., Rao, R., Rodríguez, L. F., & Torrelles, J. M. 2018, *ApJ*, 856, L27
- Güdel, M., Audard, M., Skinner, S. L., & Horvath, M. I. 2002, *ApJ*, 580, L73
- Güdel, M. & Benz, A. O. 1993, *ApJ*, 405, L63
- Hales, C. A., Murphy, T., Curran, J. R., Middelberg, E., Gaensler, B. M., & Norris, R. P. 2012, *MNRAS*, 425, 979
- Hanson, M. M., Howarth, I. D., & Conti, P. S. 1997, *ApJ*, 489, 698
- Hoffmeister, V. H., Chini, R., Scheyda, C. M., Schulze, D., Watermann, R., Nürnberger, D., & Vogt, N. 2008, *ApJ*, 686, 310
- Holwerda, B. W. 2005, arXiv e-prints, astro
- Jiang, Z., Yao, Y., Yang, J., Ando, M., Kato, D., Kawai, T., Kurita, M., Nagata, T., Nagayama, T., Nakajima, Y., Nagashima, C., Sato, S., Tamura, M., Nakaya, H., & Sugitani, K. 2002, *ApJ*, 577, 245
- Johnson, C. O., De Pree, C. G., & Goss, W. M. 1998, *ApJ*, 500, 302
- Kounkel, M., Hartmann, L., Loinard, L., Mioduszewski, A. J., Dzib, S. A., Ortiz-León, G. N., Rodríguez, L. F., Pech, G., Rivera, J. L., Torres, R. M., Boden, A. F., Evans, II, N. J., Briceño, C., & Tobin, J. 2014, *ApJ*, 790, 49
- Kounkel, M., Hartmann, L., Loinard, L., Ortiz-León, G. N., Mioduszewski, A. J., Rodríguez, L. F., Dzib, S. A., Torres, R. M., Pech, G., Galli, P. A. B., Rivera, J. L., Boden, A. F., Evans, Neal J., I., Briceño, C., & Tobin, J. J. 2017, *ApJ*, 834, 142
- Lada, C., Dickinson, D. F., & Penfield, H. 1974, *ApJ*, 189, L35
- Lim, W., De Buizer, J. M., & Radomski, J. T. 2020, *ApJ*, 888, 98
- Lugo, J., Lizano, S., & Garay, G. 2004, *ApJ*, 614, 807
- McMullin, J. P., Waters, B., Schiebel, D., Young, W., & Golap, K. 2007, in *Astronomical Society of the Pacific Conference Series*, Vol. 376, *Astronomical Data Analysis Software and Systems XVI*, ed. R. A. Shaw, F. Hill, & D. J. Bell, 127
- Medina, S. N. X., Dzib, S. A., Tapia, M., Rodríguez, L. F., & Loinard, L. 2018, *A&A*, 610, A27
- Medina, S. N. X., Urquhart, J. S., Dzib, S. A., Brunthaler, A., Cotton, B., Menten, K. M., Wyrowski, F., Beuther, H., Billington, S. J., Carrasco-Gonzalez, C., Csengeri, T., Gong, Y., Hofner, P., Nguyen, H., Ortiz-León, G. N., Ott, J., Pandian, J. D., Roy, N., Sarkar, E., Wang, Y., & Winkel, B. 2019, *A&A*, 627, A175
- Morales, E. F. E., Wyrowski, F., Schuller, F., & Menten, K. M. 2013, *A&A*, 560, A76

- Nielbock, M., Chini, R., Hoffmeister, V. H., Scheyda, C. M., Steinacker, J., Nürnberger, D., & Siebenmorgen, R. 2007, *ApJ*, 656, L81
- Nielbock, M., Chini, R., Jütte, M., & Manthey, E. 2001, *A&A*, 377, 273
- Ortiz-León, G. N., Loinard, L., Mioduszewski, A. J., Dzib, S. A., Rodríguez, L. F., Pech, G., Rivera, J. L., Torres, R. M., Boden, A. F., Hartmann, L., Evans, Neal J., I., Briceño, C., Tobin, J., Kounkel, M. A., & González-Lópezlira, R. A. 2015a, *ApJ*, 805, 9
- . 2015b, *ApJ*, 805, 9
- Panagia, N. & Felli, M. 1975, *A&A*, 39, 1
- Pech, G., Loinard, L., Dzib, S. A., Mioduszewski, A. J., Rodríguez, L. F., Ortiz-León, G. N., Rivera, J. L., Torres, R. M., Boden, A. F., Hartmann, L., Kounkel, M. A., Evans, Neal J., I., Briceño, C., Tobin, J., & Zapata, L. A. 2016, *ApJ*, 818, 116
- Povich, M. S., Churchwell, E., Bieging, J. H., Kang, M., Whitney, B. A., Brogan, C. L., Kulesa, C. A., Cohen, M., Babler, B. L., Indebetouw, R., Meade, M. R., & Robitaille, T. P. 2009, *ApJ*, 696, 1278
- Reynolds, S. P. 1986, *ApJ*, 304, 713
- Rodríguez, L. F., González, R. F., & Montes, G. 2009, *Rev. Mexicana Astron. Astrofis.*, 45, 273
- Rodríguez, L. F., González, R. F., Montes, G., Asiri, H. M., Raga, A. C., & Cantó, J. 2012, *ApJ*, 755, 152
- Rodríguez, L. F., Martí, J., Canto, J., Moran, J. M., & Curiel, S. 1993, *Rev. Mexicana Astron. Astrofis.*, 25, 23
- Rodriguez-Gomez, V., Snyder, G. F., Lotz, J. M., Nelson, D., Pillepich, A., Springel, V., Genel, S., Weinberger, R., Tacchella, S., Pakmor, R., Torrey, P., Marinacci, F., Vogelsberger, M., Hernquist, L., & Thilker, D. A. 2019, *MNRAS*, 483, 4140
- Sánchez-Monge, Á., Pandian, J. D., & Kurtz, S. 2011, *ApJ*, 739, L9
- Shull, J. M. 1980, *ApJ*, 238, 860
- Stecklum, B., Henning, T., Feldt, M., Hayward, T. L., Hoare, M. G., Hofner, P., & Richter, S. 1998, *AJ*, 115, 767
- Wang, Y., Bihl, S., Rugel, M., Beuther, H., Johnston, K. G., Ott, J., Soler, J. D., Brunthaler, A., Anderson, L. D., Urquhart, J. S., Klessen, R. S., Linz, H., McClure-Griffiths, N. M., Glover, S. C. O., Menten, K. M., Bigiel, F., Hoare, M., & Longmore, S. N. 2018, *A&A*, 619, A124
- Wu, Y. W., Sato, M., Reid, M. J., Moscadelli, L., Zhang, B., Xu, Y., Brunthaler, A., Menten, K. M., Dame, T. M., & Zheng, X. W. 2014, *A&A*, 566, A17
- Zapata, L. A., Rodríguez, L. F., Kurtz, S. E., & O'Dell, C. R. 2004, *AJ*, 127, 2252

This 2-column preprint was prepared with the AAS L^AT_EX macros v5.2.

A. Catalog of the compact radio sources of M17

Table 8:: Parameters of the CRSs with their counterparts at other wavelengths.

ID #	α (J2000)	δ (J2000)	S_{peak} ($\mu Jy beam^{-1}$)	S_{int} (μJy)	X-ray ^a	IR ^b	Optical ^c	Radio ^d
1	18 20 16.402 ± 0.002	-16 11 18.81 ± 0.03	149 ± 30	179 ± 30				
2	18 20 16.405 ± 0.002	-16 11 10.73 ± 0.03	143 ± 29	169 ± 30				
3	18 20 17.569 ± 0.001	-16 12 21.49 ± 0.02	188 ± 25	543 ± 118				
4	18 20 18.968 ± 0.002	-16 11 27.98 ± 0.03	88 ± 17	185 ± 19				
5	18 20 19.417 ± 0.001	-16 12 15.74 ± 0.01	549 ± 36	549 ± 36	✓			
6	18 20 20.722 ± 0.001	-16 08 27.79 ± 0.02	177 ± 29	241 ± 30	✓	✓	✓	
7	18 20 21.433 ± 0.001	-16 12 06.75 ± 0.02	180 ± 17	192 ± 17	✓	✓		4
8	18 20 21.636 ± 0.001	-16 11 17.91 ± 0.01	286 ± 22	400 ± 25		✓	✓	5
9	18 20 21.736 ± 0.001	-16 11 12.59 ± 0.01	222 ± 17	227 ± 16				
10	18 20 21.849 ± 0.002	-16 09 05.43 ± 0.03	72 ± 15	94 ± 15				
11	18 20 21.921 ± 0.002	-16 13 33.15 ± 0.03	201 ± 41	211 ± 41				
12	18 20 22.339 ± 0.001	-16 11 28.55 ± 0.02	97 ± 15	189 ± 17				
13	18 20 22.358 ± 0.001	-16 07 49.51 ± 0.01	187 ± 38	474 ± 44				
14	18 20 22.363 ± 0.001	-16 12 04.87 ± 0.001	242 ± 19	242 ± 19	✓			6
15	18 20 22.468 ± 0.002	-16 09 51.39 ± 0.03	55 ± 10	58 ± 10	✓			
16	18 20 22.852 ± 0.001	-16 11 48.51 ± 0.02	171 ± 15	239 ± 17	✓			
17	18 20 23.082 ± 0.001	-16 13 05.23 ± 0.02	244 ± 29	270 ± 29				
18	18 20 23.107 ± 0.002	-16 13 01.91 ± 0.03	123 ± 24	125 ± 24	✓			
19	18 20 23.157 ± 0.002	-16 13 05.67 ± 0.03	134 ± 27	134 ± 27	✓			
20	18 20 23.181 ± 0.001	-16 10 43.47 ± 0.02	119 ± 14	137 ± 15				
21	18 20 23.763 ± 0.001	-16 11 57.99 ± 0.02	112 ± 16	458 ± 27				
22	18 20 24.821 ± 0.001	-16 11 35.08 ± 0.01	18582 ± 1003	97836 ± 5092	✓	✓		UC1
23	18 20 24.897 ± 0.001	-16 10 42.56 ± 0.02	122 ± 15	122 ± 15	✓			
24	18 20 25.318 ± 0.001	-16 11 48.64 ± 0.02	230 ± 29	892 ± 65				7
25	18 20 25.496 ± 0.002	-16 10 53.80 ± 0.03	90 ± 17	207 ± 20	✓	✓		8
26	18 20 25.622 ± 0.002	-16 09 37.04 ± 0.03	45 ± 9	62 ± 9				
27	18 20 25.847 ± 0.001	-16 08 32.16 ± 0.03	87 ± 13	93 ± 13	✓	✓	✓	
28	18 20 26.116 ± 0.002	-16 09 13.92 ± 0.03	46 ± 9	100 ± 10				
29	18 20 26.216 ± 0.001	-16 09 21.52 ± 0.02	70 ± 10	85 ± 10			✓	
30	18 20 26.240 ± 0.001	-16 11 15.84 ± 0.01	270 ± 21	345 ± 41		✓		10
31	18 20 27.379 ± 0.001	-16 11 38.56 ± 0.01	262 ± 18	565 ± 30				12
32	18 20 27.588 ± 0.001	-16 11 33.40 ± 0.01	886 ± 49	886 ± 49	✓		✓	
33	18 20 27.615 ± 0.001	-16 10 43.32 ± 0.03	45 ± 7	48 ± 7	✓	✓	✓	
34	18 20 27.715 ± 0.001	-16 09 51.12 ± 0.02	79 ± 8	99 ± 8	✓	✓		
35	18 20 27.742 ± 0.002	-16 14 16.76 ± 0.03	252 ± 49	340 ± 51				
36	18 20 27.798 ± 0.001	-16 08 57.76 ± 0.02	87 ± 11	87 ± 11	✓	✓	✓	
37	18 20 27.857 ± 0.001	-16 09 55.64 ± 0.02	79 ± 8	89 ± 8	✓	✓	✓	13
38	18 20 28.023 ± 0.001	-16 11 26.96 ± 0.01	208 ± 14	274 ± 16				14
39	18 20 28.034 ± 0.001	-16 10 42.36 ± 0.02	79 ± 7	80 ± 7				
40	18 20 28.151 ± 0.001	-16 10 49.32 ± 0.03	41 ± 7	72 ± 7	✓	✓	✓	
41	18 20 28.154 ± 0.002	-16 10 01.00 ± 0.03	31 ± 6	31 ± 6				
42	18 20 28.206 ± 0.002	-16 11 05.64 ± 0.03	37 ± 7	37 ± 7				
43	18 20 28.231 ± 0.001	-16 13 17.80 ± 0.01	1627 ± 89	1674 ± 85	✓	✓		15
44	18 20 28.273 ± 0.001	-16 10 42.36 ± 0.01	117 ± 8	151 ± 9				
45	18 20 28.287 ± 0.001	-16 11 30.56 ± 0.02	128 ± 13	172 ± 14	✓	✓		16
46	18 20 28.367 ± 0.001	-16 10 30.68 ± 0.02	43 ± 6	43 ± 6	✓	✓	✓	
47	18 20 28.384 ± 0.001	-16 10 14.16 ± 0.01	164 ± 11	222 ± 13				17
48	18 20 28.487 ± 0.001	-16 10 39.56 ± 0.01	99 ± 8	108 ± 8				
49	18 20 28.503 ± 0.001	-16 10 55.36 ± 0.02	58 ± 7	226 ± 13				
50	18 20 28.548 ± 0.001	-16 10 26.84 ± 0.01	110 ± 8	149 ± 10				
51	18 20 28.720 ± 0.001	-16 10 22.16 ± 0.03	47 ± 6	47 ± 6				
52	18 20 28.787 ± 0.002	-16 11 51.92 ± 0.03	40 ± 9	48 ± 8				
53	18 20 28.787 ± 0.001	-16 10 49.32 ± 0.02	63 ± 6	71 ± 7				
54	18 20 28.798 ± 0.001	-16 11 03.68 ± 0.03	41 ± 7	41 ± 7				
55	18 20 28.839 ± 0.001	-16 10 56.08 ± 0.02	72 ± 7	72 ± 7	✓	✓		
56	18 20 28.867 ± 0.001	-16 11 10.08 ± 0.03	42 ± 6	42 ± 6	✓	✓		

Table 8 – Parameters of the CRSs with their counterparts at other wavelengths.

ID #	α (J2000)	δ (J2000)	S_{peak} ($\mu Jy beam^{-1}$)	S_{int} (μJy)	X-ray ^a	IR ^b	Optical ^c	Radio ^d
57	18 20 28.998 ± 0.001	-16 10 33.44 ± 0.03	37 ± 6	54 ± 6				
58	18 20 29.139 ± 0.001	-16 12 09.84 ± 0.03	50 ± 9	101 ± 10				
59	18 20 29.167 ± 0.001	-16 09 43.04 ± 0.01	124 ± 9	156 ± 10	✓	✓	✓	
60	18 20 29.192 ± 0.001	-16 10 54.68 ± 0.01	28 ± 6	28 ± 6				
61	18 20 29.217 ± 0.001	-16 10 38.80 ± 0.02	49 ± 6	61 ± 6				
62	18 20 29.231 ± 0.002	-16 11 03.00 ± 0.03	34 ± 6	51 ± 6				
63	18 20 29.267 ± 0.001	-16 10 41.32 ± 0.01	83 ± 7	83 ± 7	✓	✓	✓	
64	18 20 29.317 ± 0.001	-16 10 47.96 ± 0.03	50 ± 6	51 ± 6	✓			
65	18 20 29.317 ± 0.001	-16 09 50.60 ± 0.03	36 ± 6	41 ± 6				
66	18 20 29.323 ± 0.002	-16 10 18.08 ± 0.03	31 ± 6	77 ± 7				
67	18 20 29.367 ± 0.001	-16 11 08.88 ± 0.01	90 ± 8	90 ± 8				
68	18 20 29.386 ± 0.002	-16 09 43.00 ± 0.03	34 ± 6	126 ± 9	✓	✓		
69	18 20 29.436 ± 0.001	-16 10 49.84 ± 0.01	283 ± 16	656 ± 33	✓			19
70	18 20 29.445 ± 0.002	-16 09 16.64 ± 0.03	39 ± 8	51 ± 8				
71	18 20 29.495 ± 0.002	-16 08 04.00 ± 0.03	77 ± 16	101 ± 16				
72	18 20 29.625 ± 0.002	-16 11 41.56 ± 0.03	35 ± 6	37 ± 6				
73	18 20 29.728 ± 0.001	-16 10 59.92 ± 0.03	48 ± 7	57 ± 7				
74	18 20 29.731 ± 0.001	-16 11 04.48 ± 0.02	46 ± 6	60 ± 7				
75	18 20 29.736 ± 0.001	-16 10 53.40 ± 0.01	121 ± 9	131 ± 9				
76	18 20 29.745 ± 0.001	-16 09 55.64 ± 0.02	52 ± 6	60 ± 6				
77	18 20 29.750 ± 0.002	-16 11 25.76 ± 0.03	29 ± 6	34 ± 6				
78	18 20 29.767 ± 0.001	-16 10 44.72 ± 0.02	45 ± 6	45 ± 6				
79	18 20 29.811 ± 0.001	-16 10 45.56 ± 0.01	692 ± 38	891 ± 45	✓			20 (CEN 1b)
80	18 20 29.822 ± 0.001	-16 11 11.80 ± 0.02	60 ± 6	60 ± 6				
81	18 20 29.828 ± 0.001	-16 10 48.32 ± 0.01	109 ± 8	109 ± 8				
82	18 20 29.842 ± 0.001	-16 10 40.72 ± 0.02	46 ± 6	59 ± 7	✓			
83	18 20 29.842 ± 0.001	-16 10 31.04 ± 0.01	137 ± 9	198 ± 12				
84	18 20 29.850 ± 0.001	-16 10 41.20 ± 0.01	230 ± 14	230 ± 14	✓			
85	18 20 29.861 ± 0.001	-16 10 44.72 ± 0.01	173 ± 11	177 ± 11				
86	18 20 29.897 ± 0.001	-16 10 44.44 ± 0.01	566 ± 31	566 ± 31	✓			21 (CEN 1a)
87	18 20 29.911 ± 0.002	-16 10 35.08 ± 0.03	30 ± 6	30 ± 6	✓			
88	18 20 29.917 ± 0.001	-16 10 33.60 ± 0.02	74 ± 7	81 ± 7				
89	18 20 29.925 ± 0.001	-16 09 14.64 ± 0.01	39 ± 7	49 ± 8				
90	18 20 29.953 ± 0.001	-16 10 50.80 ± 0.02	85 ± 7	94 ± 7				
91	18 20 29.953 ± 0.002	-16 10 33.76 ± 0.03	32 ± 6	32 ± 6				
92	18 20 29.968 ± 0.001	-16 11 15.36 ± 0.01	77 ± 7	78 ± 7				
93	18 20 29.989 ± 0.001	-16 10 44.68 ± 0.02	44 ± 6	79 ± 7				
94	18 20 30.003 ± 0.001	-16 10 35.28 ± 0.01	514 ± 28	627 ± 32	✓			22
95	18 20 30.031 ± 0.001	-16 10 34.68 ± 0.02	79 ± 7	79 ± 7				
96	18 20 30.042 ± 0.002	-16 11 57.44 ± 0.03	35 ± 7	35 ± 7	✓	✓	✓	
97	18 20 30.044 ± 0.002	-16 10 33.40 ± 0.03	32 ± 6	34 ± 6				
98	18 20 30.094 ± 0.001	-16 10 41.44 ± 0.02	44 ± 6	54 ± 6	✓			
99	18 20 30.133 ± 0.001	-16 10 39.48 ± 0.01	307 ± 17	404 ± 21				23
100	18 20 30.178 ± 0.001	-16 11 20.08 ± 0.02	58 ± 6	58 ± 6				
101	18 20 30.194 ± 0.002	-16 10 50.48 ± 0.03	34 ± 6	34 ± 6	✓			
102	18 20 30.208 ± 0.001	-16 10 12.04 ± 0.01	85 ± 7	89 ± 7				
103	18 20 30.278 ± 0.001	-16 11 31.48 ± 0.03	37 ± 6	49 ± 6	✓	✓	✓	
104	18 20 30.286 ± 0.001	-16 10 39.52 ± 0.03	34 ± 6	48 ± 6				
105	18 20 30.325 ± 0.001	-16 10 50.68 ± 0.01	186 ± 11	198 ± 11				24
106	18 20 30.380 ± 0.002	-16 11 44.20 ± 0.03	28 ± 6	32 ± 6				
107	18 20 30.394 ± 0.001	-16 10 52.64 ± 0.03	39 ± 6	48 ± 6				
108	18 20 30.414 ± 0.001	-16 11 03.64 ± 0.01	179 ± 11	218 ± 13				26
109	18 20 30.436 ± 0.001	-16 11 01.56 ± 0.02	91 ± 8	105 ± 9				
110	18 20 30.444 ± 0.001	-16 10 53.12 ± 0.01	152 ± 10	153 ± 10	✓	✓	✓	27
111	18 20 30.450 ± 0.001	-16 10 10.08 ± 0.03	35 ± 5	78 ± 6	✓	✓	✓	
112	18 20 30.530 ± 0.002	-16 11 51.40 ± 0.03	32 ± 6	42 ± 6				
113	18 20 30.541 ± 0.001	-16 10 39.56 ± 0.02	46 ± 6	53 ± 6				
114	18 20 30.575 ± 0.001	-16 10 30.96 ± 0.03	36 ± 6	47 ± 6				
115	18 20 30.578 ± 0.001	-16 11 04.16 ± 0.01	606 ± 33	670 ± 35		✓		28
116	18 20 30.633 ± 0.002	-16 10 28.52 ± 0.03	27 ± 5	27 ± 5	✓	✓		29

Table 8 – Parameters of the CRSs with their counterparts at other wavelengths.

ID #	α (J2000)	δ (J2000)	S_{peak} ($\mu Jy beam^{-1}$)	S_{int} (μJy)	X-ray ^a	IR ^b	Optical ^c	Radio ^d
117	18 20 30.664 ± 0.001	-16 10 44.24 ± 0.03	35 ± 6	46 ± 6				
118	18 20 30.678 ± 0.001	-16 10 50.12 ± 0.02	61 ± 6	73 ± 7				
119	18 20 30.711 ± 0.001	-16 10 31.96 ± 0.02	45 ± 6	45 ± 6				
120	18 20 30.777 ± 0.001	-16 10 59.36 ± 0.01	585 ± 32	826 ± 42	✓			30
121	18 20 30.780 ± 0.001	-16 11 00.24 ± 0.01	29 ± 6	75 ± 7				
122	18 20 30.811 ± 0.001	-16 10 41.60 ± 0.02	61 ± 6	61 ± 6	✓			
123	18 20 30.850 ± 0.001	-16 10 48.76 ± 0.02	74 ± 7	166 ± 10				
124	18 20 30.877 ± 0.002	-16 09 05.04 ± 0.03	40 ± 8	44 ± 8	✓	✓	✓	
125	18 20 30.894 ± 0.001	-16 09 54.80 ± 0.02	60 ± 6	84 ± 7	✓	✓	✓	
126	18 20 30.908 ± 0.001	-16 11 35.96 ± 0.03	34 ± 6	38 ± 6	✓	✓	✓	
127	18 20 30.911 ± 0.001	-16 10 39.48 ± 0.01	98 ± 7	135 ± 9	✓	✓		
128	18 20 31.111 ± 0.001	-16 09 29.84 ± 0.01	147 ± 10	147 ± 10	✓	✓	✓	31
129	18 20 31.305 ± 0.001	-16 10 50.96 ± 0.02	39 ± 5	39 ± 5	✓			
130	18 20 31.336 ± 0.001	-16 10 52.80 ± 0.02	38 ± 5	41 ± 5				
131	18 20 31.355 ± 0.001	-16 10 57.84 ± 0.01	125 ± 8	130 ± 8				
132	18 20 31.424 ± 0.002	-16 11 03.48 ± 0.03	28 ± 5	28 ± 6				
133	18 20 31.433 ± 0.001	-16 10 31.00 ± 0.01	75 ± 6	93 ± 7				
134	18 20 31.469 ± 0.001	-16 09 13.08 ± 0.03	47 ± 8	74 ± 8				
135	18 20 31.477 ± 0.002	-16 09 48.76 ± 0.03	28 ± 6	32 ± 6				
136	18 20 31.516 ± 0.001	-16 09 10.40 ± 0.02	65 ± 8	78 ± 8	✓		✓	
137	18 20 31.527 ± 0.002	-16 10 32.60 ± 0.03	28 ± 5	39 ± 6	✓	✓		32
138	18 20 31.602 ± 0.001	-16 11 05.88 ± 0.02	58 ± 6	58 ± 6				
139	18 20 31.641 ± 0.002	-16 10 36.72 ± 0.03	28 ± 6	44 ± 6				
140	18 20 31.716 ± 0.001	-16 11 06.80 ± 0.03	39 ± 6	39 ± 6				
141	18 20 31.883 ± 0.001	-16 11 24.04 ± 0.03	34 ± 6	42 ± 6	✓	✓		
142	18 20 31.977 ± 0.001	-16 09 25.16 ± 0.02	55 ± 7	55 ± 7	✓	✓		
143	18 20 31.999 ± 0.002	-16 11 27.00 ± 0.03	30 ± 6	32 ± 6	✓			
144	18 20 32.002 ± 0.002	-16 09 40.44 ± 0.03	31 ± 6	41 ± 6				
145	18 20 32.324 ± 0.001	-16 10 48.92 ± 0.01	92 ± 7	102 ± 7				
146	18 20 32.521 ± 0.002	-16 11 11.04 ± 0.03	32 ± 6	32 ± 6				
147	18 20 32.549 ± 0.002	-16 10 06.20 ± 0.03	27 ± 5	38 ± 5				
148	18 20 32.688 ± 0.002	-16 10 20.16 ± 0.03	26 ± 5	32 ± 5				
149	18 20 32.932 ± 0.001	-16 10 35.68 ± 0.02	46 ± 6	46 ± 6				
150	18 20 32.979 ± 0.001	-16 11 15.56 ± 0.01	107 ± 8	117 ± 8				33
151	18 20 33.060 ± 0.001	-16 11 21.60 ± 0.01	642 ± 35	642 ± 35	✓	✓		34
152	18 20 33.093 ± 0.001	-16 09 40.80 ± 0.01	153 ± 10	739 ± 37				35
153	18 20 33.199 ± 0.002	-16 11 20.84 ± 0.03	29 ± 6	29 ± 6				
154	18 20 33.247 ± 0.001	-16 13 22.92 ± 0.03	109 ± 18	109 ± 18				
155	18 20 33.324 ± 0.002	-16 11 11.00 ± 0.03	25 ± 5	25 ± 5				
156	18 20 33.398 ± 0.002	-16 10 18.44 ± 0.03	29 ± 5	34 ± 6				
157	18 20 33.404 ± 0.001	-16 09 44.40 ± 0.02	65 ± 7	77 ± 7				
158	18 20 33.438 ± 0.002	-16 10 55.32 ± 0.03	29 ± 6	72 ± 7				
159	18 20 33.504 ± 0.001	-16 10 44.60 ± 0.01	235 ± 14	352 ± 18				36
160	18 20 33.610 ± 0.001	-16 10 21.68 ± 0.01	115 ± 8	136 ± 9				37
161	18 20 33.768 ± 0.001	-16 10 46.44 ± 0.01	127 ± 9	176 ± 10				38
162	18 20 34.059 ± 0.001	-16 10 28.88 ± 0.02	50 ± 6	65 ± 7				
163	18 20 34.079 ± 0.001	-16 10 44.52 ± 0.01	83 ± 7	91 ± 7	✓	✓	✓	
164	18 20 34.209 ± 0.002	-16 10 21.36 ± 0.03	29 ± 6	53 ± 6				
165	18 20 34.576 ± 0.001	-16 10 23.44 ± 0.01	85 ± 7	93 ± 7				
166	18 20 34.673 ± 0.001	-16 11 23.40 ± 0.02	67 ± 7	79 ± 7				
167	18 20 34.888 ± 0.002	-16 13 47.60 ± 0.03	160 ± 32	213 ± 33				
168	18 20 35.048 ± 0.001	-16 09 48.28 ± 0.02	79 ± 8	135 ± 10				
169	18 20 35.197 ± 0.001	-16 09 49.64 ± 0.02	72 ± 8	121 ± 9				
170	18 20 35.479 ± 0.001	-16 11 11.84 ± 0.02	75 ± 7	77 ± 7	✓	✓	✓	
171	18 20 35.858 ± 0.002	-16 10 18.95 ± 0.03	37 ± 7	69 ± 8				
172	18 20 36.238 ± 0.002	-16 08 57.43 ± 0.03	54 ± 11	54 ± 11				
173	18 20 36.449 ± 0.002	-16 08 17.03 ± 0.03	87 ± 17	167 ± 19				
174	18 20 36.879 ± 0.001	-16 12 14.91 ± 0.02	99 ± 11	232 ± 15				
175	18 20 37.762 ± 0.002	-16 08 43.03 ± 0.03	75 ± 15	83 ± 15				
176	18 20 37.803 ± 0.002	-16 11 53.83 ± 0.03	53 ± 10	58 ± 10				

Table 8 – *Parameters of the CRSs with their counterparts at other wavelengths.*

ID	α		δ		S_{peak}	S_{int}	X-ray ^a	IR ^b	Optical ^c	Radio ^d
#	(J2000)		(J2000)		($\mu Jy beam^{-1}$)	(μJy)				
177	18	20	37.895 ± 0.002	-16 12	19.99 ± 0.03	57 ± 12				
178	18	20	39.819 ± 0.002	-16 11	37.47 ± 0.03	57 ± 12				
179	18	20	40.895 ± 0.002	-16 10	08.46 ± 0.03	67 ± 14				
180	18	20	40.984 ± 0.002	-16 10	08.30 ± 0.03	71 ± 14				
181	18	20	43.625 ± 0.002	-16 10	38.57 ± 0.03	133 ± 26				
182	18	20	44.343 ± 0.002	-16 10	09.77 ± 0.03	207 ± 38				

^a Chandra X-ray Observatory, (Broos et al. 2007)

^b Two Micron All-Sky Survey, Spitzer Space Telescope Galactic Legacy infrared Mid-Plane survey. IR counterparts are reported when the sources are detected at least at one of the available bands.

^c Gaia Data Release 2.

^d Catalog number in RGM2012.